INCORPORATION OF HYSTERETIC EFFECTS IN MODEL-ORDER REDUCTION ANALYSIS OF MAGNETIC DEVICES

BY

JONATHAN JOSEPH SANDER

B.S., University of Illinois at Urbana-Champaign, 2007

THESIS

Submitted in partial fulfillment of the requirements
for the degree of Master of Science in Electrical and Computer Engineering
in the Graduate College of the
University of Illinois at Urbana-Champaign, 2009

Urbana, Illinois

Adviser:

Associate Professor Patrick L. Chapman

ABSTRACT

The ability to predict the properties of magnetic materials in a device is essential to ensuring the correct operation and optimization of the design as well as the device behavior over a wide range of input frequencies. Typically, development and simulation of wide-bandwidth models requires detailed, physics-based simulations that utilize significant computational resources. Balancing the trade-offs between model computational overhead and accuracy can be cumbersome, especially when the nonlinear effects of saturation and hysteresis are included in the model.

This study focuses on the development of a system for analyzing magnetic devices in cases where model accuracy and computational intensity must be carefully and easily balanced by the engineer. A method for adjusting model complexity and corresponding level of detail while incorporating the nonlinear effects of hysteresis is presented that builds upon recent work in loss analysis and magnetic equivalent circuit (MEC) modeling. The approach utilizes MEC models in conjunction with linearization and model-order reduction techniques to process magnetic devices based on geometry and core type. The validity of steady-state permeability approximations is also discussed.

To my family, for their love and support

TABLE OF CONTENTS

LIST OF TABLES

LIST OF FIGURES

CHAPTER 1

INTRODUCTION

Several different methods for magnetic analysis that utilize various models of hysteretic phenomena have been presented in recent work. Because of the wide variation in approaches, a distinction must be made between the analysis methods used on a magnetic device and the models used to identify the magnetic phenomena, particularly hysteresis. In some cases, the model and the method are closely intertwined and cannot be discussed separately, while other methods allow virtually any hysteresis model to be used in the analysis.

Two of the more popular models will be discussed in Chapter 2, but most can be broken down into time-based systems with "memory" or those based on sets of partial differential equations. In many cases, the models can be generalized to any hysteretic phenomena, relying on additional methods to extrapolate to the magnetic domain and any simplifying assumptions associated with it.

When reduced-order models are considered, incorporation of nonlinear effects becomes difficult due to the inability to predict the trajectory of the system in a time-based simulation. State-space models present a more difficult problem in the frequency domain, since the response becomes characterized by the magnitude of the input in addition to the frequency. Up to a linear approximation, nonlinear systems can easily be reduced using quasi pole-zero cancellation or other linear reduction techniques such as Kron reduction or Krylov subspaces. However, the validity of a linearized model must first be confirmed to ensure that accuracy is maintained after reduction.

Two particular magnetic analysis methods were considered for this work, both of which will be discussed briefly as a comparison.

1.1 Previous Work in Model-Order Reduction Techniques

1.1.1 FEA reduced-order modeling

Finite element analysis has traditionally been a widely used method for modeling of electric machinery due to its scalability and accuracy. However, computer simulations can quickly become cumbersome both in setup and computational overhead when real magnetic devices are considered. Additionally, the solutions of electric and magnetic fields at the domain boundaries require time-based simulation which can obscure some of the more desirable characteristics of the system that a simple state-space model can quickly provide. Of course, when nonlinear effects are incorporated, the frequency response of the system becomes less important as only time-domain simulation can extract the effects in a meaningful manner, making FEA an attractive candidate for these situations.

Recent work in FEA has focused on addressing the computational resources required for developing a model while retaining the high level of accuracy that is characteristic of physics-based models. In [1], a high-level discussion of model-order reduction methods of finite element models is presented which incorporates advancements in system development and simplification. Several methods were used for model-order reduction including a trajectory piecewise-linear (TPWL) approach and Krylov subspace techniques [2]. Typically, some combination of linearization and reduction must take place when incorporating nonlinear effects.

Hysteresis became the focus in [3] via the inverse Preisach model, with the limitation of time-based simulation associated with that particular model, which will

be discussed in Chapter 2. While state-space methods are still heavily employed for model-development, the tracking of hysteretic state must be done in the time-domain – again, a condition usually required of hysteretic models, but without the flexibility of frequency based simulation for a given input amplitude.

An improvement was made in MOR techniques in [1] and [4] where quasi pole-zero cancellation and Kron reduction were utilized to bring the number of states in the system down by two orders of magnitude while still maintaining good levels of accuracy and bandwidth. The model was linearized around a series of steady-state points and proceeded with order reduction from there. While linearization around all sets of approximate steady-sate values could potentially be slow, the method utilized training to only linearize around new points as the model approached them. When the system's state passes through those points during subsequent intervals, the previously reduced system may be used. Exceptional gains in simulation time were made and while this concept requires the assumption of steady-state currents and fluxes, it can be very effective while maintaining accuracy with empirical results.

1.1.2 MEC reduced-order modeling

An analogous approach to FEA also exists for magnetic equivalent circuit analysis. In [5], an induction machine model is built on a series of permeance elements called flux tubes. Each flux tube can be associated with a reluctance value based on geometry and magnetic state, if hysteresis is included in the model. Similarly to FEA, each flux tube has a magnetic potential defined at each boundary, with a corresponding flux flowing between each boundary transverse to the surface. A magnetic device can then be built using a network of permeance elements covering the relevant surfaces and structures in and around the device, analogous to the meshing process in FEA. Leakage flux surrounding the device can easily be incorporated in the model by

adding flux tubes in the air gaps (or other surrounding areas) and using the appropriate magnetic properties of the medium.

For simplicity and speed of simulation, a sensible selection of permeance elements consists of the main flux paths throughout the length of the device about its axis of symmetry. While this method relies on the device being symmetrical, in machine and inductor analysis this is often the case. In a simple toroidal configuration with an air gap, the flux tubes can be defined about the axial direction of the device even though the medium itself is not continuous over that path. In this case additional elements need to be inserted into the path to represent the new medium with a permeability of free space, and correspond to series reluctance elements in the complete network model.

This approach contains an additional subtle assumption disallowing any leakage flux from a flux tube. No fringing effects may occur within the device when the flux tubes represent continuous paths throughout, an assumption that reduces accuracy, particularly around corner points and interfaces between unlike media. Work in [6] and [7] attempts to overcome this limitation by breaking the flux tubes into multiple permeance elements, representing series reluctances in the equivalent circuit model. While this complicates the model, it illustrates the scalability of MEC analysis to handle virtually the same tasks as FEA, even in three dimensions, while offering the desired level of accuracy as well.

The analysis in [8] extrapolated MEC circuits to incorporate eddy current modeling in conjunction with model-order reduction. Eddy currents can be modeled as inductive elements in the MEC circuit, maintaining linearity and allowing for linear reduction techniques to be applied. By simplifying parallel and series reluctances and permeances, the network model reduces to a simple state-space system. Quasi pole-zero cancellation proved effective at reducing systems from hundreds of state variables to less than ten while maintaining accuracy over a bandwidth of megahertz.

1.2 Approach

This thesis builds on the progress made using MEC with model-order reduction techniques. The development of the state-space system with eddy current is outlined and expanded to include hysteretic effects. Linearization techniques applied to the resulting system allow for model-order reduction while maintaining accuracy in simulation. A first attempt is made at reducing the system under constant flux-tube permeability across the device geometry and yields the results presented. An investigation into the validity of this assumption follows with a more accurate representation of varying permeabilities throughout the reluctance network. While this method requires significantly more computation, it incorporates the variance in permeabilities between flux tubes associated with differing geometries and corresponding flux densities.

CHAPTER 2

HYSTERESIS MODELS

Many models exist for describing the effects of hysteresis on magnetic devices and elsewhere in nature [9]. Recent work focuses primarily on two models, Preisach and Jiles-Atherton, depending on what type of analysis methods are utilized and the compatibility and ease of implementation with the system. For this work, the hysteresis model does not directly depend on the simulation method since the nonlinearities are removed prior to simulation through linearization and model-order reduction. However, other methods incorporate the hysteresis model directly, requiring compatibility and ideally seamless introduction to the model. Since both models were considered, a brief development is presented to illustrate the differences and provide guidance on their selection.

2.1 Preisach Model

The Preisach model was first introduced in 1938 and has since become touted as one of the most accurate models of hysteresis due to its physical basis. The building blocks of the model focus on individual magnetic moments, called hysterons, which approximate the natural phenomenon at one of the lowest levels. The major challenge in understanding and implementing the model occurs in the geometrical interpretation of the Preisach domain, the fundamental concept of the model [10].

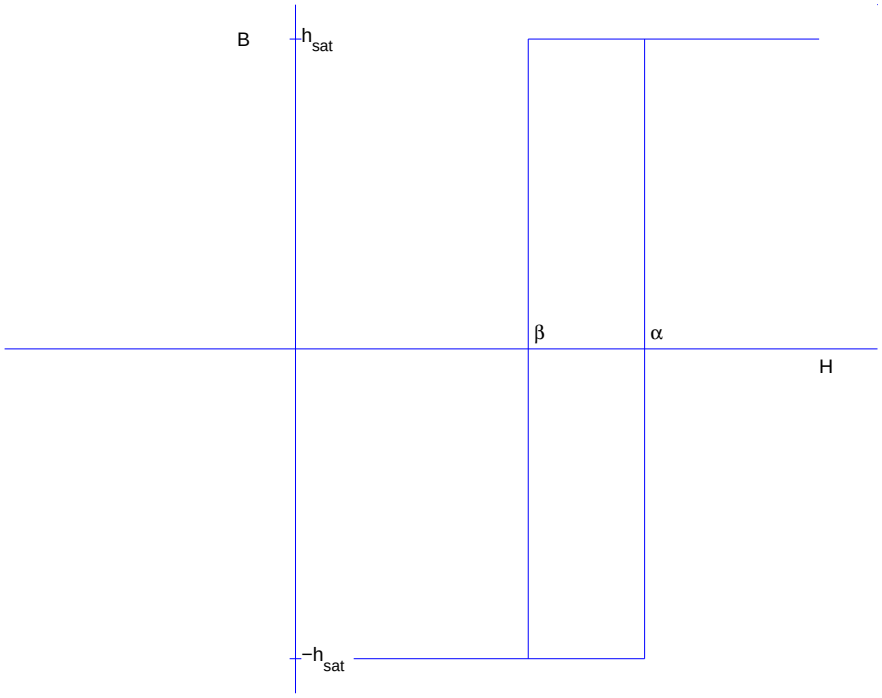

Figure 2.1: A hysteron element with magnetic states of $\pm h_{sat}$ (= 1) and reversal points of α and β. Note that $\alpha \geq \beta$ for all elements.

2.1.1 Background

The widely recognized theory behind magnetic effects including para- and ferromagnetism incorporates the idea of magnetic domains which can alter their orientation in the presence of magnetic field, either enhancing or mitigating the overall effect, depending on the type of material. The Preisach model includes this effect by introducing hysterons and defining a few key properties, illustrated in Figure 2.1.

Each hysteron represents a single magnetic domain with two states, h_{sat} and $-h_{sat}$, where h_{sat} is simply unity, representing alignment or antialignment with an applied field. The geometric interpretation of hysterons carries with it a few important implications:

1. Hysterons are in either a positive or a negative (up or down) state, exclusively.

2. Flux applied at either threshold value will result in a state change, if applicable (e.g., the hysteron is not already in the resulting state).

3. The positive switching threshold, α, is greater than the negative switching threshold, β, for all hysterons.

The combination of these properties defines a new space in the 2-D plane, known as the Priesach domain. This domain receives information about the flux through the device and reorients individual hysterons' magnetic polarity based on the distribution of switching values.

2.1.2 The Preisach domain

The hysteron properties correspond to the bounded region shown in Figure 2.2, known as the limiting triangle. The coordinate system is split into the α and β axes and defined by the positive saturation value, negative saturation value, and the region $\alpha \geq \beta$ as per rule 3. The domain itself effectively stores the individual hysterons and their switching values at their respective locations in the plane, based on their α, β coordinate position, most often taken from a desired statistical distribution as outlined in Section 2.1.3. Each hysteron resides at some Boolean magnetic state, up or down, until a field change beyond the switching value is applied. In the case of a down-state hysteron, application of positive field beyond the α value will cause the hysteron to flip into the up-state and vice versa for a transition from the up-state. The distribution of all of the hysteron states in the system can be graphically represented as a horizontal or vertical line in the domain, bisecting the region into two additional regions. The area above and to the right of the bisecting boundary corresponds to all of the hysterons in the down-state, while the region below and to the left of the boundary represents those in the up-state. The up-state and down-state regions are typically denoted as S^+ and S^-, respectively. At any given time, the magnetic state of

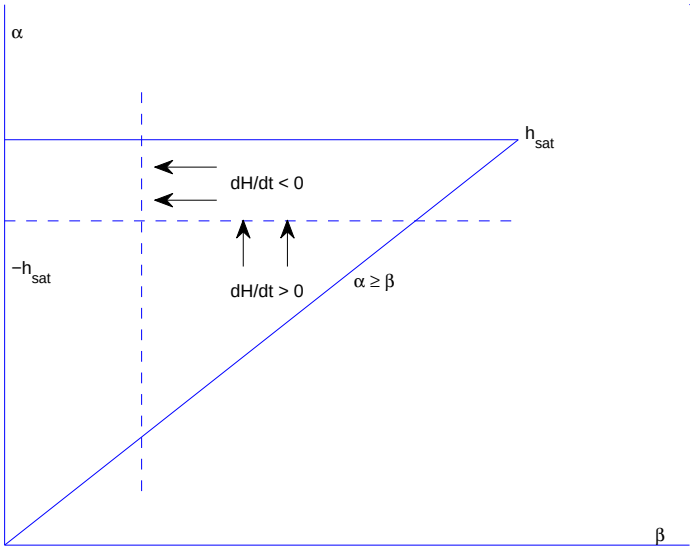

Figure 2.2: Graphical representation of the Preisach domain. Increasing positive flux corresponds to a change in boundaries along the vertical α axis while decreasing flux results in horizontal movement of the boundary along the β axis.

the material can be determined by summing the number of up-state hysterons and subtracting the total down-state hysterons.

As expected, the behavior of the model has incorporated the value of the applied field by comparison with the switching limits of each hysteron. Additionally, we would expect the model to be defined by the field direction, intuitively corresponding to the up or down branch on the hysteresis loop. We do this by the addition of two final rules to the model:

1. Increasing positive flux results in movement of the horizontal domain boundary along an upward trajectory.

2. Decreasing flux results in the movement of the vertical domain boundary along a horizontal trajectory to the left.

The domain boundary movement can be thought of as a broom sweeping across the

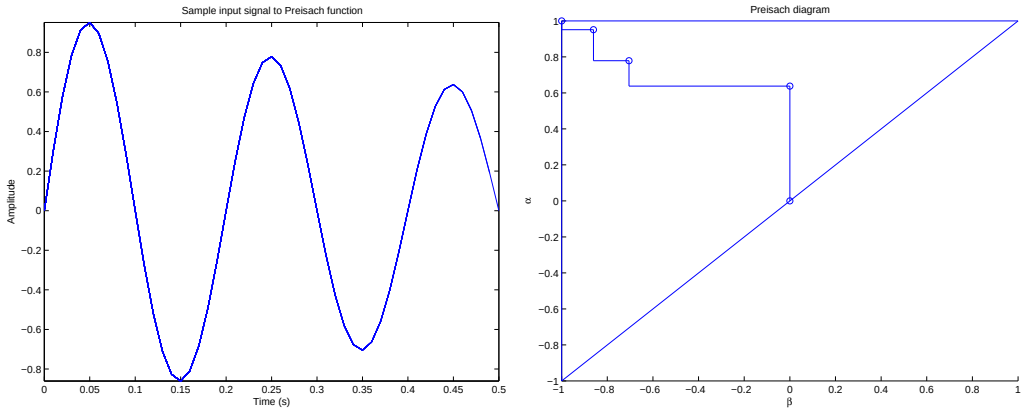

(a) (b)

Figure 2.3: Sample input signal of a decaying sinusoid into the Preisach function (a) and the resulting boundary line in the Preisach domain (b).

region, flipping the state of each hysteron that it crosses, except that the boundary is limited to only two possible directions: left or up. In the case of increasing field, the width of the boundary extends from the $\alpha = \beta$ line on the right to the most recent vertical boundary on the left. Regardless of the applied field strength, the boundary proceeds upward from the bottom vertex of the region and flips each hysteron along it to the up-state until either saturation is reached or the field direction changes. Thus, if a nonzero sliver of down-state hysterons exists prior to the boundary movement, the complete removal of the domain's memory requires positive field application until saturation. Decreasing field causes the opposite boundary movement. A vertical boundary line begins from the most recent horizontal point achieved and extends downward to the $\alpha \geq \beta$ line until saturation or a direction change. This combination of movements and boundary changes produces knees in the boundary line with vertices located at (M_k, m_k).

The input signal in Figure 2.3 illustrates the effects of field changes to the boundary line in the Preisach domain. Each critical point in the input function directly correlates to a knee in the boundary line with the inclusion of the line's endpoints as products of the first and last critical points. The first horizontal step results from the

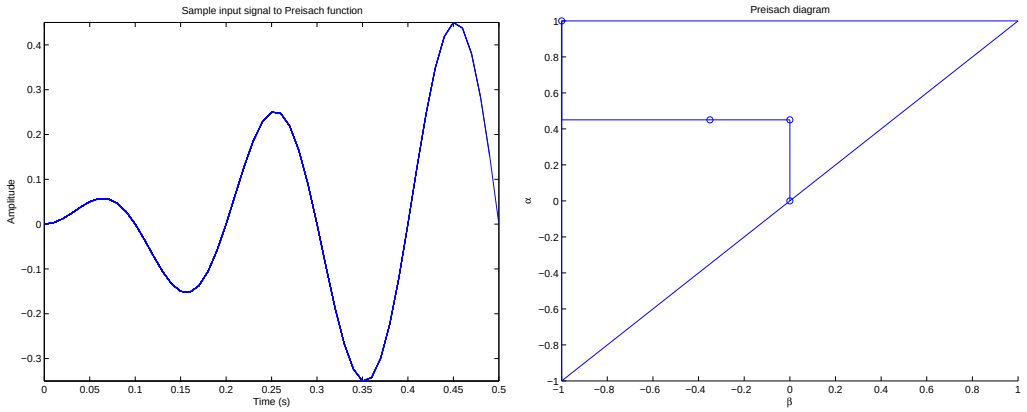

(a) (b)

Figure 2.4: Sample input signal of an increasing sinusoid into the Preisach function (a) and the resulting boundary line in the Preisach domain (b), illustrating the wiping of memory in the system.

input increasing up to the first peak and changing direction. This change in direction sweeps the first vertical bar in from the right, stopping when the first trough is reached. A second horizontal line moves upward along the new vertical, and so on. A decaying sinusoid illustrates this concept well due to the fact that each successive peak or trough is smaller in magnitude than the previous. If a pure sinusoid were used, the boundary movement in the Preisach domain would be obscured, appearing as the same two horizontal and vertical lines oscillating back and forth. A growing sinusoid may be used to illustrate the memory wiping property of the system as seen in Figure 2.4. Very little activity can be viewed in the single snapshot of the Preisach domain because all of the previous reversal points have been overwritten and wiped clean from the domain. For illustrative purposes, the previous knee markers recorded by the input peaks can be seen where they would reside had they not been wiped by the last peak.

2.1.3 Implementation

Once the domain boundary is established, the hysteron states need to be combined to form the total magnetization state of the material. Calculating the geometric area of

each subdomain and subtracting the negative or down-state hysterons from the positive, up-state hysterons represents the simplest method for using the Preisach domain to calculate magnetization state. A constant weighting factor could be used to amplify or reduce the total magnetization as needed, simulating multiple hysterons at each switching value combination in the plane.

We define $\hat{\gamma}$ as the value of an individual hysteron, up or down, functionally dependent on the *total* input, $u(t)$, as opposed to only the most recent input, based on the boundary line path. Mathematically, the hysteron operator becomes

$$\hat{\gamma}_{\alpha,\beta}(u(t)) = \begin{cases} +1, & \text{in } S^+ \\ -1, & \text{in } S^- \end{cases} \tag{2.1}$$

with a weighting function of ν. Again, a simple area calculation for S^+ and S^- produces the magnetization state, or mathematically,

$$f(t) = S^+ - S^- = \nu \sum_{k=1}^{p-1} F_k \tag{2.2}$$

where F_k is the value of an individual trapezoid created by a knee in the boundary line and p is the total number of trapezoids. Letting f_α denote the value associated with a limiting horizontal branch from an increasing input $u = \alpha$ and $f_{\alpha\beta}$ be the output of the reversal in the decreasing direction from α to $u = \beta$, we can then write the total output of the function as

$$f(t) = -f^+ + \sum_{k=1}^{p-1} (f_{M_k m_k} - f_{M_k m_{k-1}}) + f_{M_p u(t)} - f_{M_p m_{p-1}} \tag{2.3}$$

Thus far we have used a constant factor to represent hysteron distribution for convenience, but this is certainly not the case for real magnetic materials, nor is it physically meaningful in the model. Instead, the weighting factor should consist of a function in the $\alpha - \beta$ plane, preferably based on a suitable statistical distribution. In

this case, the output value function in (2.3) becomes an integral over the distribution function in the entire Preisach domain,

$$f(t) = \int\int_{\alpha \geq \beta} \nu(\alpha, \beta) \hat{\gamma}_{\alpha\beta}(u(t)) d\alpha d\beta \tag{2.4}$$

$$\nu(\alpha, \beta) = \frac{1}{2\pi\sigma_i\sigma_k} \exp\left[-\frac{(\alpha+\beta)^2}{8\sigma_i^2} - \frac{(\alpha-\beta)-(\bar{\alpha}-\bar{\beta})}{4\sigma_k^2} \right] \tag{2.5}$$

Recent efforts have focused on identifying appropriate statistical distributions for various materials as well as methods to assign distributions based on material parameters [11]. As an example, a Gaussian hysteron distribution given by (2.5) appears in Figure 2.5 projected onto the Preisach domain. At each time step, the boundary line will be fixed and the function integrated over the surface, requiring piecewise integration for each trapezoidal region. Additionally, the upper and lower boundaries of the Preisach domain no longer apply as the distribution extends outwards to infinity. However, piecewise integration at each time step over the function in (2.5) can be cumbersome, so many efforts have been made to reduce the complexity of the Preisach function, including discretized domains and averaging techniques [10].

Figure 2.6 illustrates a complete hysteresis model using the Preisach method. The model includes minor loops from field reversals made prior to saturation quite well and requires no additional effort to incorporate. A characteristic feature of a major hysteresis loop developed by the Preisach model is the horizontal asymptote reached quickly with saturation field. This arises in part from the truncation of the statistical model at the saturation boundaries of the Preisach domain and needs to be compensated for in models where operation in saturation conditions are likely to occur. Simply setting a fixed saturation permeability above a certain applied field value provides a simple enough solution. The challenge of matching material

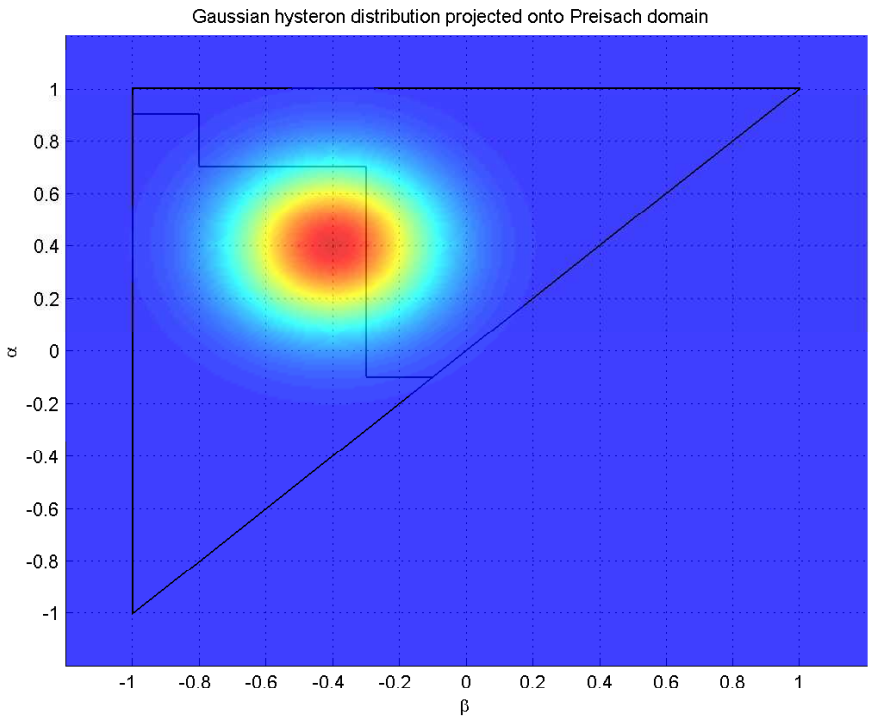

(a)

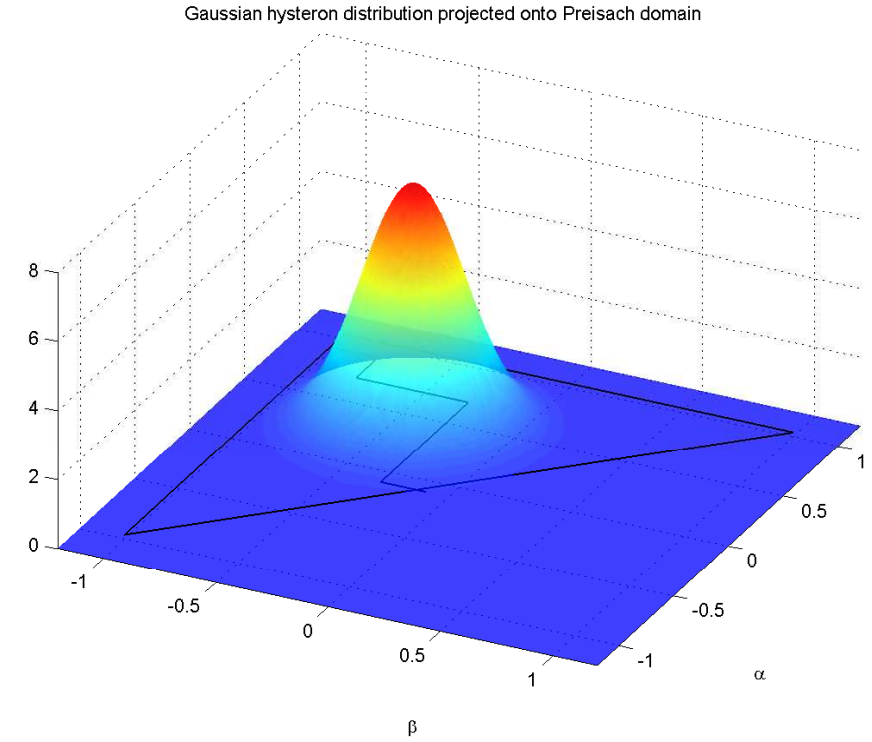

(b)

Figure 2.5: A Gaussian hysteron distribution projected onto the Preisach domain from above (a) and the side (b).

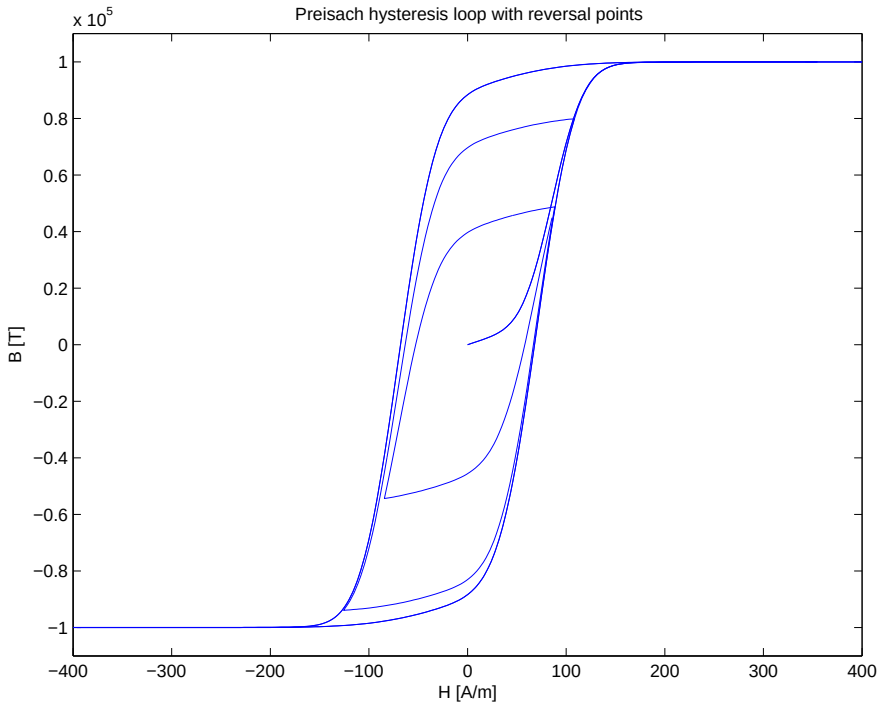

Figure 2.6: Preisach hysteresis loop with minor loops from reversals.

parameters to a theoretical Preisach loop remains a point of discussion. Inverse Preisach modeling offers methods for loop identification from empirical measurements, and efforts have been made to simplify the procedures while maintaining accuracy [12], [13]. Additionally, work done in [14] identifies a method for incorporating the frequency dependence of the hysteresis loop into the model.

2.1.4 Vector models

The Preisach model as described has a significant limitation in the scalar nature of the system: magnetic fields can affect the hysterons only in a single direction. Any vector components of field off of the primary axis will not be accounted for in the switching states. To overcome this, work has been done on vector Preisach models in [15] and [10] involving an additional integral term to (2.4) to account for directionality of the field. The integral is taken over the right half-plane since negative field direction is

compensated for in the hysteron switching states. The result,

$$f(t) = \int_{\pi/2}^{\pi/2} e_{\phi} \left(\int \int_{\alpha \geq \beta} \nu(\alpha, \beta) \hat{\gamma}_{\alpha\beta}(u(t)) d\alpha d\beta \right) d\phi \tag{2.6}$$

requires another integration over an already potentially complicated piecewise surface distribution. Fortunately, additional analysis in the same papers offer a means of applying empirical measurements to a new function, $P(\alpha, \beta)$, which simplifies the numerical integration significantly. For the work presented here, a vectorial model is not considered and is left as an exercise for future efforts.

2.2 Jiles-Atherton

The Jiles-Atherton hysteresis model was introduced in [16] and concerns itself with the interaction of individual domain boundaries and their rotations in addition to mutual interaction with neighboring domains. The model identifies the present magnetism of the material as a state variable and proceeds through a series of nonlinear partial differential equations describing the major and minor loops at reversal points.

2.2.1 State equations

The model begins by separating the magnetic state into an anhysteretic and reversible component,

$$M = M_{irr} + M_{rev} \tag{2.7}$$

with some forms of the equation adjusting the contribution of each component by a weighting factor to account for domain flexing [17],

$$M = (c)M_{irr} + (1-c)M_{rev} \tag{2.8}$$

Regardless of the placement, the domain flexing parameter will affect the model by scaling the reversible component. The flux density retains the well-known constitutive relation while the effective field is adjusted by a material-varying constant, α,

$$H_e = H + \alpha M \tag{2.9}$$

$$B = \mu_0(H + M) \tag{2.10}$$

The irreversible component is given by the partial differential equation

$$\frac{dM_{irr}}{dH} = \frac{M_{an} - M_{irr}}{\delta^* k - \alpha(M_{an} - M_{irr})} \tag{2.11}$$

where $\delta = \text{sign}\left(\frac{dH}{dt}\right)$ accounts for the flux direction and we have yet to define the anhysteretic component, M_{an}. The reversible component, as mentioned, contains the domain flexing scaling factor, c, which adjusts the distance of the irreversible component from the static, anhysteretic curve or, mathematically,

$$M_{rev} = c(M_{an} - M_{irr}), \tag{2.12}$$

which results in the differential equation

$$\frac{dM_{rev}}{dH} = c\left(\frac{dM_{an}}{dH} - \frac{dM_{irr}}{dH}\right) \tag{2.13}$$

Combining Equations (2.7), (2.11), and (2.13) produces the final Jiles-Atherton differential equation for magnetization,

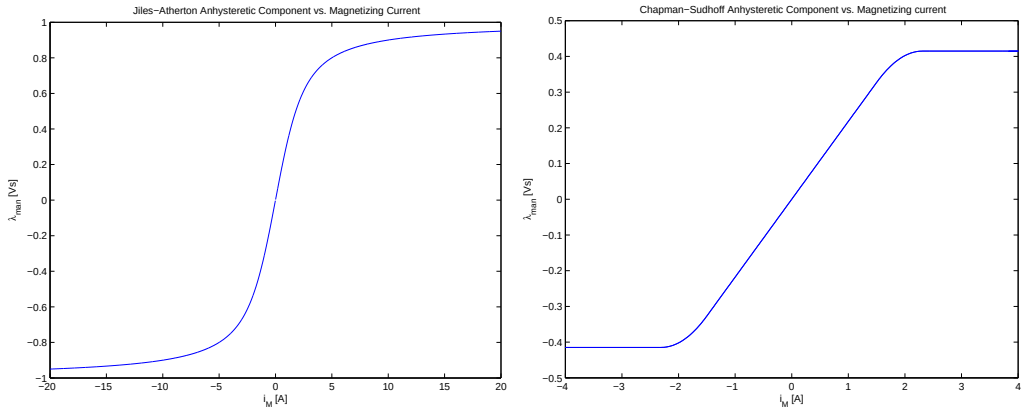

(a) (b)

Figure 2.7: Two possible choices for the Jiles-Atherton anhysteretic function. The Langevin function (a) was originally published with the model while (b) was a piecewise option presented in [18].

$$\frac{dM}{dH} = \frac{1}{(1+c)} \frac{(M_{an} - M)}{\delta^* k - \alpha(M_{an} - M)} + \frac{c}{(1+c)} \frac{dM_{an}}{dH} \tag{2.14}$$

where the only quantity left to define is the constant anhysteretic function. The form of this curve effectively defines the shape of the hysteresis loop and, with some caution, can be selected by the designer to produce models that most accurately match empirical results. The Jiles-Atherton model was originally proposed using the Langevin function,

$$M_{an} = M_s \left(\coth \left(\frac{H_e}{a} - \frac{a}{H_e} \right) \right) \tag{2.15}$$

with a being a material parameter empirically determined. Up to a constant, the function can be plotted against magnetizing current for simplicity, with the results in Figure 2.7.

Other anhysteretic functions have been suggested not only due to matching of material characteristics, but also to avoid discontinuities and the associated problems with the Langevin function. Special care must be taken around the zero current point in simulation, a precaution that may not be necessary with other anhysteretic models.

One such model presented in [18] breaks the anhysteretic component into a piecewise function consisting of

$$\lambda_{M_{an}} = \begin{cases} L_{M_i} i_M & 0 \leq i_M < i_L \\ \frac{-L_{M_i}\left(\frac{1}{2} i_M^2 - i_H i_M\right)}{i_H - i_L} + \lambda_{MC} & i_L \leq i_M < i_H \\ \lambda_{M_s} & i_H \leq i_M \end{cases} \tag{2.16}$$

with

$$\lambda_{MC} = L_{M_i}\left(i_L + \frac{\frac{1}{2} i_L^2 - i_L i_H}{i_H i_L}\right) \tag{2.17}$$

chosen for continuity and the magnetization current constants chosen to provide the desired interconnecting points. It has been presented here as it appeared in the paper where flux linkage was used instead of magnetization, but the general curve retains its shape as seen in Figure 2.7.

2.2.2 Implementation

With the state equations in place, the solution to the magnetization of the material can be obtained by numerically integrating (2.14) using any method of choice so long as stability is maintained. A sample hysteresis loop was made for various input fields in Figure 2.8. Note that the model predicts minor loops at the reversal points in addition to the major hysteresis loop, and unlike the Preisach model, the upper and lower limits of the slope never reach the horizontal asymptote that they appear to approach. Parameter identification is equally important and has been the focus of considerable research [19], [20], [21]. Methods of matching M_s, a, α, c, and k typically involve an iterative numerical method whereby an error function is minimized on certain trajectories associated with some, but not all, of the variables.

Like the Preisach model, the Jiles-Atherton model can be extended to include vector

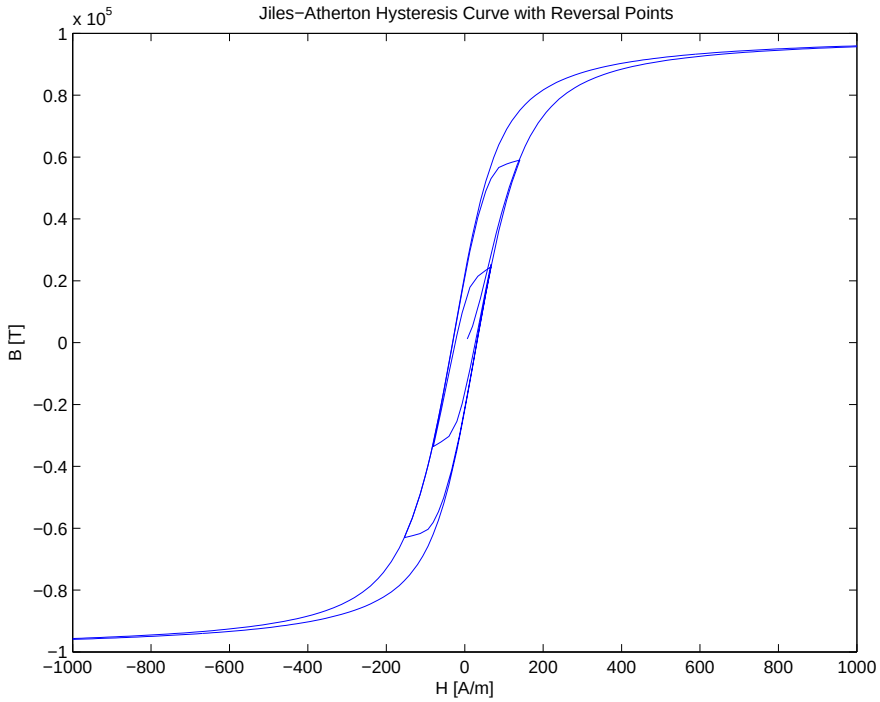

Figure 2.8: Jiles-Atherton hysteresis loop with minor loops from reversals.

components of magnetic field, as well as inverse methods to assist in back-calculating model parameters from experimental data [22], [23].

CHAPTER 3

MEC MODEL DEVELOPMENT

As mentioned previously, this work builds on that presented in [24] and, as a result, the development of the MEC models utilizing flux tube networks is discussed and the basic theory redeveloped. The simplest model consists of continuous flux tubes excluding eddy current losses and is presented as the basis for further development. The addition of eddy current losses maintains linearity in the system allowing for the construction of a state-space model to be built upon later. Although frequency domain analysis cannot be well defined for nonlinear methods, it provides a starting point for inclusion of hysteresis under the most basic assumptions of homogeneous, but nonlinearly varying permeability to be discussed subsequently.

3.1 Flux Tube Circuit Equations

In order to model the response of a magnetic device to an input current or voltage, the coupling between the electric and magnetic domains must be considered in any model. To achieve this, a modeling device known as a magneto-electric differential gyrator is used as an interface between classical electrical circuit components and their magnetic equivalent counterparts. A schematic of the gyrator appears in Figure 3.1 and illustrates the cross-coupling of current and flux into each domain. The device can be described completely by two voltage loops on either side of the coupling,

$$V_{in} = R_{ext} i_{in} + L_{ext} \frac{di_{in}}{dt} + N \frac{d\phi}{dt} \tag{3.1}$$

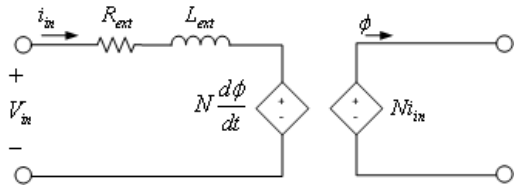

Figure 3.1: Circuit model showing coupling between the electric and magnetic domains.

$$Ni_{in} = \phi\mathcal{R} \tag{3.2}$$

where $\mathcal{R}$ represents the magnetic reluctance of an arbitrary terminal circuit. The parameters R_{ext} and L_{ext} are typically used as wire winding resistance and inductance and can be taken from circuit measurements.

The terminating reluctance network provides the interface from the coupling mechanism to the model generated from the system of flux tubes, ideally automated based on material properties and geometry [24], [1]. Figure 3.2 shows a 3-D section of a toroidal core, illustrating a sample arrangement of flux tubes fed by the outer winding at the face of the image. The square symmetry of the geometry in the azimuthal direction as referenced around the face breaks the cross section into zones carrying eddy current, which is covered in the following section. For now, we focus on the individual, continuous flux tubes, each carrying a flux, $\phi_{i,j}$, with reluctance,

$$\mathcal{R}_{i,j} = \frac{l_{i,j}}{\mu A_{i,j}} \tag{3.3}$$

It is important to note that the reluctance of each flux tube varies with its geometry, in this case as a function of the height from the center or vertical position, j. The corresponding circuit consists of the combined parallel reluctance of the flux tubes, shown in Figure 3.3, which can be simplified to a single equivalent reluctance. Neglecting wire inductance, we can rewrite Equation (3.1) as

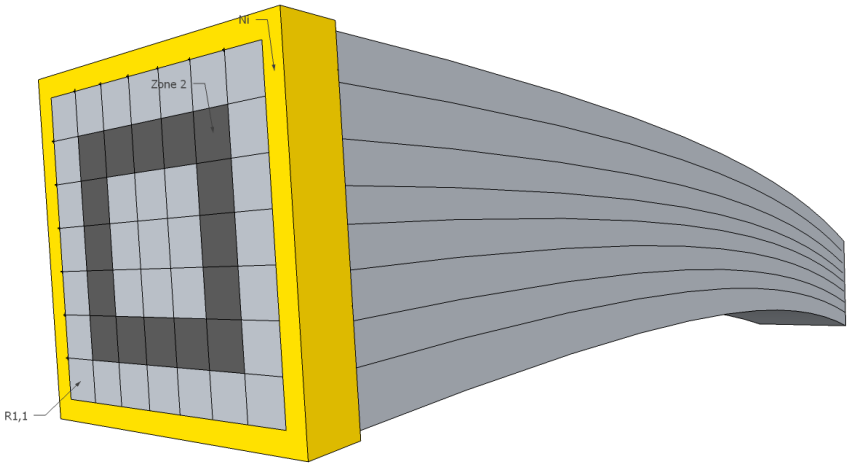

Figure 3.2: 3-D representation of flux tubes in a section of a toroidal core.

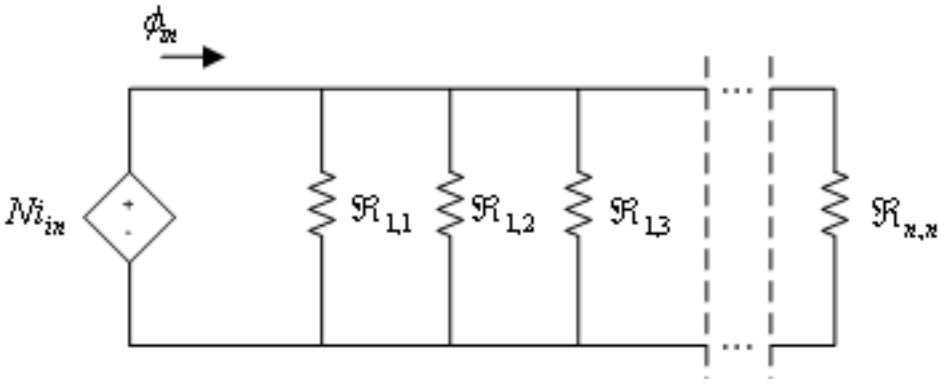

Figure 3.3: Equivalent circuit representation of flux tubes.

$$\frac{d\phi}{dt} = \frac{V_{in}}{N} - \frac{R_{ext} i_{in}}{N}$$

We can take advantage of the magnetic-electric coupling by substituting for i_{in} using (3.2), resulting in

$$\frac{d\phi}{dt} = \frac{V_{in}}{N} - \frac{R_{ext}\mathcal{R}\phi}{N^2}$$

and we can replace $\frac{d\phi}{dt}$ with $\dot{\phi}$ to put the equation into state-space notation:

$$\dot{\phi} = \left[-\frac{R_{ext}\mathcal{R}}{N^2}\right]\phi + \left[\frac{1}{N}\right]V_{in}$$

A state-space system may seem to be overkill for such a simple system consisting of only a single variable, but organizing state variables becomes important as complexity is added to the system, as we will see in the next section. Inclusion of winding inductance would add the inductor current as another state variable, but this exercise is left to the reader. To finish the state-space system, we must identify the output variable of interest, in this case the total input current, i_{in}. We can refer to Equation (3.2) for the simplest relationship to our state variable, ϕ,

$$i = \left[\frac{\mathcal{R}}{N}\right]\phi$$

resulting in the final system

$$\dot{x} = \left[-\frac{R_{ext}\mathcal{R}}{N^2}\right]x + \left[\frac{1}{N}\right]u \tag{3.4}$$

$$y = \left[\frac{\mathcal{R}}{N}\right]x \tag{3.5}$$

where x is the scalar flux, ϕ, u represents the input voltage, V_{in}, and y outputs the

resulting system current, i_{in}. The system reflects the input-output relationship, $\frac{i_{in}}{V_{in}}$, which physically corresponds to the overall input admittance of the system, Y_{in}.

3.2 Incorporation of Eddy Currents

Extending the model to include eddy currents added significant value to the MEC model while managing to retain the simplicity of the model and the ability to scale to more complicated systems [25]. The development begins with the definition of eddy current paths, called zones, which group flux tubes in concentric rings within the core, as seen in Figure 3.4. Each flux tube contributes to a total lateral conductance for each ring,

$$G_{i,j} = \frac{\sigma A_{i,j}}{l_{i,j}} \tag{3.6}$$

where σ is the material conductivity along the direction of current flow. The individual conductivities are summed in series for the calculation of an equivalent conductivity for the ring, making the resistive inverse useful for practical considerations. However, once the equivalent conductivities of the rings are known, incorporation into the model requires more effort than simply placing them in series with the equivalent reluctance. In fact, we will need to break up the equivalent reluctances produced from Figure 3.3 and place them into a magnetic equivalent R-L ladder structure.

Each zone produces an equivalent reluctance to magnetic flux while the conductance of the tubes provides a path for circulating current to flow, requiring a model of this current for our magnetic domain circuit. From the coupling in Figure 3.1 or Maxwell's equations, we can determine that the relationship of the current directly corresponds to the time rate of change of magnetic flux, producing an inductive element in the magnetic domain. The resulting magnetic circuit appears in Figure 3.5 and illustrates the combination of equivalent reluctances and conductances in addition

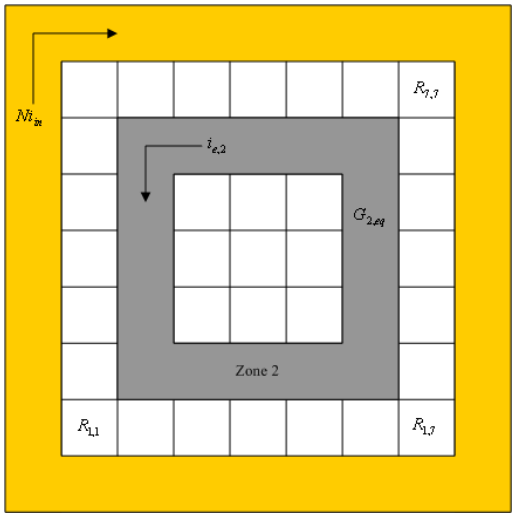

Figure 3.4: Cross-sectional view of a flux tube system with associated zones. Each zone is capable of conducting eddy currents opposing the primary current as shown.

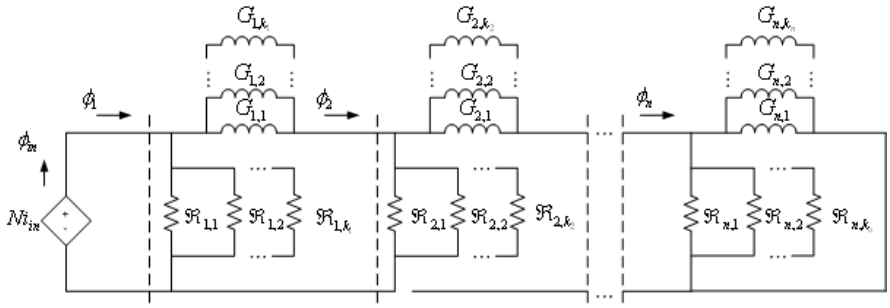

Figure 3.5: The magnetic equivalent circuit incorporating eddy currents into the model.

to their placement in the R-L ladder structure.

To analyze the circuit, we again begin with Equation (3.1) and note that each tube is now identified by the total flux entering into it, as shown in Figure 3.5. Very little changes in the original voltage loop except for the variable names and their effective values now that the zones have been separated into their individual equivalent reluctances. This results in the slightly modified version of (3.1),

$$V_{in} = R_{ext} i_{in} + \mathcal{R}_{1,eq} N \dot{\phi}_1$$

where we have again neglected wire inductance and have denoted the n-th zone

equivalent reluctance and conductance as $\mathcal{R}_{n,eq}$ and $G_{n,eq}$. Since the flux through the first reluctance branch is no longer the entire flux in the circuit, the branch flux in 3.2 must be derated by that passing to the rest of the circuit or, mathematically, $\phi = \phi_1 - \phi_2$. Using this quantity for ϕ and substituting Equation (3.2) for i_{in}, we can solve for $\dot{\phi}_1$ to get

$$\dot{\phi}_1 = -\frac{\mathcal{R}_{1,eq}R_{ext}}{N^2}\phi_1 + \frac{\mathcal{R}_{1,eq}R_{ext}}{N^2}\phi_2 + \frac{1}{N}V_{in} \tag{3.7}$$

This sets up the first entry for a state-space description of the system. It is clear that each conductance element in the network will produce an associated state variable in the form of a time-derivative flux through the element, hence the chosen definition of flux variables in Figure 3.5. We can evaluate the circuit equation of the next zone element by writing a new equation for the surrounding voltage loop,

$$\mathcal{R}_{1,eq}(\phi_1 - \phi_2) = G_{1,eq}\dot{\phi}_2 + \mathcal{R}_2(\phi_2 - \phi_3)$$

and, solving for $\dot{\phi}_2$,

$$\dot{\phi}_2 = \frac{\mathcal{R}_{1,eq}}{G_{1,eq}}\phi_1 - \frac{(\mathcal{R}_{1,eq} + \mathcal{R}_{2,eq})}{G_{1,eq}}\phi_2 + \frac{\mathcal{R}_{2,eq}}{G_{1,eq}}\phi_3 \tag{3.8}$$

where all of the flux variables are retained as shown for state-space implementation. Each state variable can be described in this manner as a function of the states in the branches on either side of it up until the terminating branch. This represents a special case where the right side flux is nonexistent and therefore takes on a zero value in the proceeding derivation. No additional equations are necessary to describe the system, since taking into account the zero from the nonexistent last branch, the branch equations (not including the initial branch) can be generalized to

$$\dot{\phi}_n = \frac{\mathcal{R}_{n-1,eq}}{G_{n-1,eq}}\phi_{n-1} - \frac{(\mathcal{R}_{n-1,eq} + \mathcal{R}_{n,eq})}{G_{n-1,eq}}\phi_n + \frac{\mathcal{R}_{n,eq}}{G_{n-1,eq}}\phi_{n+1} \tag{3.9}$$

An interesting side note can be made concerning the absence of the n-th conductance value from the state equations. Because each state depends only on on the previous conductance, the final branch conductance does not effect the overall transfer function of the system. Intuitively, this arises as a result of conductance's short-circuit connection to the ground terminal, resulting in a "no-load" dependence for the branch.

To fully specify the state-space system, the output equation must be considered. The variable of interest remains input current on the electrical side of the gyrator, and we can again use Equation (3.2) to identify its relationship to the state variables. By the same argument used to identify the input flux to the first branch, the current relationship will now depend on the difference between the first branch flux derated by that flowing to the rest of the magnetic circuit, or

$$Ni_{in} = \mathcal{R}_{1,eq}(\phi_1 - \phi_2)$$

and solving for our output variable, i_{in},

$$i_{in} = \frac{\mathcal{R}_{1,eq}}{N}\phi_1 - \frac{\mathcal{R}_{1,eq}}{N}\phi_2 \tag{3.10}$$

The final state-space description can be given by

$$\vec{\dot{x}} = \begin{bmatrix} -\frac{\mathcal{R}_{1,eq}R_{ext}}{N^2} & \frac{\mathcal{R}_{1,eq}R_{ext}}{N^2} & 0 & 0 & \cdots & 0 \\ \frac{\mathcal{R}_{1,eq}}{G_{1,eq}} & -\frac{(\mathcal{R}_{1,eq}+\mathcal{R}_{2,eq})}{G_{1,eq}} & \frac{\mathcal{R}_{2,eq}}{G_{1,eq}} & 0 & \cdots & \vdots \\ 0 & \ddots & \ddots & \ddots & \ddots & \vdots \\ 0 & 0 & \ddots & \ddots & \ddots & 0 \\ \vdots & \vdots & \ddots & \ddots & \ddots & \frac{\mathcal{R}_{n,eq}}{G_{n-1,eq}} \\ 0 & \cdots & \cdots & 0 & \frac{\mathcal{R}_{n-1,eq}}{G_{n-1,eq}} & -\frac{(\mathcal{R}_{n-1,eq}+\mathcal{R}_{n,eq})}{G_{n,eq}} \end{bmatrix} \vec{x} + \begin{bmatrix} \frac{1}{N} \\ 0 \\ \vdots \\ \vdots \\ \vdots \\ 0 \end{bmatrix} V_{in} \tag{3.11}$$

$$\vec{y} = i_{in} = \begin{bmatrix} \frac{\mathcal{R}_{1,eq}}{N} & -\frac{\mathcal{R}_{1,eq}}{N} & 0 & \cdots & \cdots & 0 \end{bmatrix} \vec{x} \tag{3.12}$$

As an example, a simple, three-tube system would produce the state-space matrices

$$\mathbf{A} = \begin{bmatrix} -\frac{\mathcal{R}_{1,eq}R_{ext}}{N^2} & \frac{\mathcal{R}_{1,eq}R_{ext}}{N^2} & 0 \\ \frac{\mathcal{R}_{1,eq}}{G_{1,eq}} & -\frac{(\mathcal{R}_{1,eq}+\mathcal{R}_{2,eq})}{G_{1,eq}} & \frac{\mathcal{R}_{2,eq}}{G_{1,eq}} \\ 0 & \frac{\mathcal{R}_{2,eq}}{G_{2,eq}} & -\frac{(\mathcal{R}_{2,eq}+\mathcal{R}_{3,eq})}{G_{2,eq}} \end{bmatrix}$$

$$\mathbf{B} = \begin{bmatrix} \frac{1}{N} \\ 0 \\ 0 \end{bmatrix}, \mathbf{C} = \begin{bmatrix} \frac{\mathcal{R}_{1,eq}}{N} & -\frac{\mathcal{R}_{1,eq}}{N} & 0 \end{bmatrix}, \mathbf{D} = \mathbf{0}$$

3.3 Model-Order Reduction

The results in [8] focus on the reduction of the network built in the previous sections. Any useful model will consist of n number of zones, depending on the size of the device, with the number of flux tubes increasing as n^2. Each flux tube contributes a state to the overall model, resulting in a rapidly growing system that may become difficult to simulate. Fortunately, the developed state-space system contains only fixed

values, allowing for linear model-order reduction techniques to be employed. In [8], the primary method consisted of quasi pole-zero cancellation which proved effective due to the close proximities of the flux tube reluctances and conductances. Each tube varies only along the radial axis of the toroid and does so at a modestly linear rate. Over the effective distances within the device, the contributions produce relatively small changes, putting the pole-zero sequences close together in the s-plane. Additionally, the approximation can be adjusted for higher or lower accuracy by changing the distance between consecutive poles and zeros at which a cancellation will occur.

The state-space system formed from the flux-tube network produces another useful property in the sparsity of the A-matrix as well as the input and output vectors. The sparse, tridiagonal structure of the A-matrix allows for the straightforward implementation of additional model-order reduction techniques such as the Krylov subspace method. This method calculates the subspace,

$$K_r(\mathbf{A},\mathbf{b}) = \text{span}\left\{\mathbf{b},\mathbf{A}\mathbf{b},\mathbf{A}^2\mathbf{b},...,\mathbf{A}^{r-1}\mathbf{b}\right\}$$

from the system and input matrices [26], [27]. Each successive column vector of the span brings the system closer to linear independence, with the last vector achieving linear independence exactly. However, the column vectors quickly approach pseudo-independence and, similar to pole-zero cancellation, the closeness of the approximation can be adjusted to suit the simulation's needs. The chosen column vectors can then be used as the span of a new subspace of reduced order and the original system recalculated to fit within the span. Several iterative methods exist to carry out the calculations for the process including the Arnoldi, Lanczos, and generalized minimum residual (GMRES) among the most popular to date [28].

Model-order reduction at this point relies on the key assumption of constant

magnetic permeability and electrical conductivity in the device. This allows the system to be modeled purely as a function of geometry and, hence, easily reduced based on fixed poles and zeros for any given time step and input. In reality, this is not the case and while the change in conductivity may be negligible or only indirectly affected by the input voltage, the change in permeability is a highly nonlinear function of the input. Thus far, we have not included any of the effects of saturation or the underlying phenomenon, hysteresis.

CHAPTER 4

INCORPORATION OF HYSTERESIS

The preceding chapter developed the magnetic equivalent circuit model of the flux tube networks under the assumption of constant permeability made in Equation (3.3). However, a more accurate description of the flux tube network contains a slightly modified permeability element,

$$\mathcal{R}_{i,j} = \frac{l_{i,j}}{\mu(H, \frac{dH}{dt})A_{i,j}} \tag{4.1}$$

and even this form does not take into account the varying permeability of the individual flux tubes. Rather, it is assumed that, while the permeability changes as a function of current and its derivative, the permeability is constant across the device geometry for a given time step or current input. Implications of this assumption are addressed in Chapter 6.

By assuming constant permeability across the device geometry, we can refer to Equation (3.11) and make a useful observation about the system matrix: every nonzero term has an inverse dependence on a flux-tube reluctance. While each individual reluctance varies from that of its neighbors, we can remove the assumed constant permeability from the entire matrix, leaving only the geometric dependent terms. Identifying the new reluctances as $\tilde{\mathcal{R}}_{i,j}$, the resulting system would be only a slightly modified form of (3.11),

$$\mathbf{A} = \frac{1}{\mu\left(H, \frac{dH}{dt}\right)} \begin{bmatrix} -\frac{\tilde{\mathcal{R}}_{1,eq} R_{ext}}{N^2} & \frac{\tilde{\mathcal{R}}_{1,eq} R_{ext}}{N^2} & 0 & 0 & \cdots & 0 \\ \frac{\tilde{\mathcal{R}}_{1,eq}}{G_{1,eq}} & -\frac{(\tilde{\mathcal{R}}_{1,eq} + \tilde{\mathcal{R}}_{2,eq})}{G_{1,eq}} & \frac{\tilde{\mathcal{R}}_{2,eq}}{G_{1,eq}} & 0 & \cdots & \vdots \\ 0 & \ddots & \ddots & \ddots & \ddots & \vdots \\ 0 & 0 & \ddots & \ddots & \ddots & 0 \\ \vdots & \vdots & \ddots & \ddots & \ddots & \frac{\tilde{\mathcal{R}}_{n,eq}}{G_{n-1,eq}} \\ 0 & \cdots & \cdots & 0 & \frac{\tilde{\mathcal{R}}_{n-1,eq}}{G_{n-1,eq}} & -\frac{(\tilde{\mathcal{R}}_{n-1,eq} + \tilde{\mathcal{R}}_{n,eq})}{G_{n,eq}} \end{bmatrix} \tag{4.2}$$

where all of the reluctance terms, while different, represent constant geometrical terms. We note that the B-matrix of the system shares the same property,

$$\vec{y} = i_{in} = \frac{1}{\mu\left(H, \frac{dH}{dt}\right)} \begin{bmatrix} \frac{\tilde{\mathcal{R}}_{1,eq}}{N} & -\frac{\tilde{\mathcal{R}}_{1,eq}}{N} & 0 & \cdots & \cdots & 0 \end{bmatrix} \vec{x} \tag{4.3}$$

The transfer function of the system is still given by

$$\frac{I_{in}(s)}{V_{in}(s)} = \mathbf{C}\left(s\mathbf{I} - \mathbf{A}\right)^{-1}\mathbf{B} \tag{4.4}$$

so although this allows us to identify the geometric contribution towards the system, it does not allow us to make any additional assumptions about the placement of the poles and zeros. Based on the transfer function equation, the spacing of the poles and zeros is not linearly dependent on any constant coefficient terms in the matrices due to both the additive identity terms and the inversion of the resulting matrix. The permeability term in **C** could be compensated for with the use of normalizing coefficients, but that does not solve the problem created by inverting the middle term.

The result of these complicating factors requires a different approach to the incorporation of hysteresis into the model. It is desired that every state-space model be accurately approximated using some method of model-order reduction. To achieve this with a nonlinearly varying parameter, some method of linearization must be

performed on the system to put it into a form that keeps the poles and zeros in fixed locations at each point. Each model can then be reduced around the linearization point and referenced in a look-up table as needed by the simulation. To accomplish this, a well-selected linearization technique must be employed on the hysteresis curve to reduce the errors in approximation as the linearization points decrease to make gains in performance.

4.1 Fixed-Width Linearization

The simplest method of linearizing the hysteresis curve identifies linearization points at given intervals along the x-axis and throws out any data points in between. Each new x-value is then assigned its corresponding y-value from the original data set. The result can be easily implemented, but fails to consider places in the function where the rate of change is especially high. Figure 4.1 shows the approximated curves over-layed on the original. The 40-point curve matches closest by far, but requires nearly half of the original data points. Such an approximation would require the same number of reduced-order models to simulate and may prove too cumbersome for practical purposes. The 10-point approximation, while much smaller, does not match well with the corner points and the upper curve nearly cuts across the original lower curve. The 20-point approximation reduces the number of points to roughly 20% of the original value and maintains close proximity to the original curve.

To objectively compare the results of the above linearization method and those following, we need some performance metric that takes into account the differences between the curve and the approximation at each point. In this case, we take the l_2 norm of the difference between each point on the original curve and the point on the linear approximation, compute the summation across all of the norms, and divide by the total number of points on the original curve to find an average of the errors.

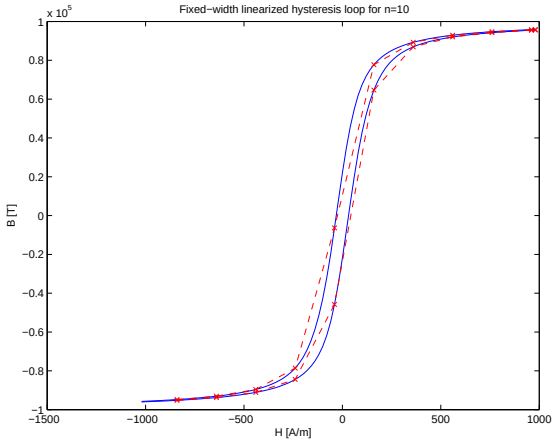

(a)

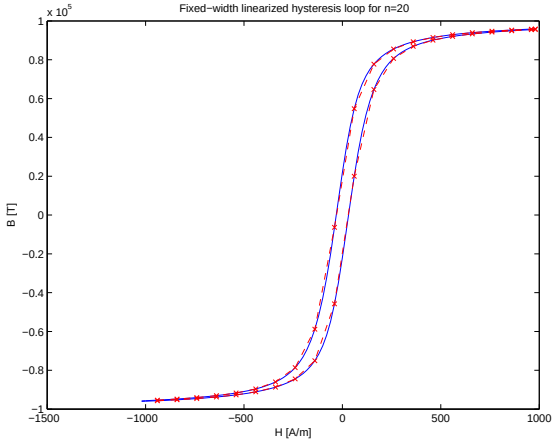

(b)

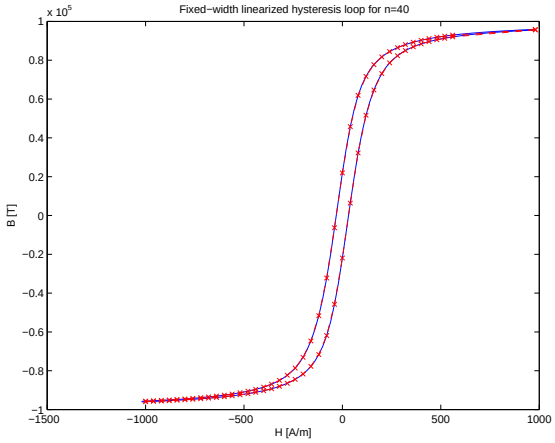

(c)

Figure 4.1: Linearized hysteresis curve using a fixed-width method for discretization up to 10 (a), 20 (b), and 40 (c) points per curve. Note that the number of points per curve represents each of the upper and lower portions of the hysteresis loop and does not include the end points.

Because the linear approximation defines only a fraction of the original curves x-values, most of the points must be calculated using a linear interpolation between successive points. This does not affect the fairness of the algorithm since each linearized curve will appear as the piecewise compilation of the points linearly interpolated as well. Additionally, there must be a metric to compare the relative performance of each linearized curve based on the number of points required and, hence, the penalty in performance with increasing points. Since the current method aims for a smaller error per point and, thus, a lower score, we can penalize higher-point linearizations by simply multiplying by the ratio of linearized points to the original number of points to create a rough metric of overall performance.

Table 4.1: Summary of the average error between each point on the original and approximated hysteresis curves using a fixed-width linearization technique.

No. of points	Avg. Error (x10^5)[T/point]	Relative Performance (x10^5) [T]
n = 10	4.42	0.44
n = 20	1.11	0.22
n = 40	0.268	0.11

Table 4.1 show the results of the linearization performance measurements. When using this metric, the 40-point method still maintains the best performance since its average error per point falls so far under the other two linearized curves. The 20-point maintains a reasonable average error, and might be preferable if performance is more important. Again, the overall performance metric is only a rough estimate requiring adjustments depending on the particular application. If performance happens to be a more important quantity, then the penalty for the number of linearization points can be increased by multiplying by the square of the points ratio or more, depending on how heavily the value needs to be weighted.

4.2 Curvature-Based Linearization

While fixed-width linearization provides an easily implemented solution to the linearization problem, it fails to account for the curvature of the function which could result in key details being omitted from the simulation. As seen in Figure 4.1 (a), a 10-point fixed-width method has the potential to skip over major curves in the function and cause large inaccuracies in the approximation line. A curvature-based method could be used to identify major changes in the slope of the hysteresis loop and increase the density of the linearization points in that region.

We can find the curvature of the hysteresis loop by first finding the slope at each point,

$$\frac{dy}{dx_i} \approx \frac{y_{i+1} - y_i}{x_{i+1} - x_i} \tag{4.5}$$

where in this case, we have made the slope calculation forward looking. Once the slopes of the curve are known, we can apply the same procedure to find the curvature at the same points. Since the slopes were calculated using a forward-looking process, we can use a backward-looking process on the derivatives to effectively make the calculation a mid-point based method,

$$\frac{d^2y}{dx_i^2} = \frac{\frac{dy}{dx_i} - \frac{dy}{dx_{i-1}}}{\frac{dy}{dx_i} - \frac{dy}{dx_{i-1}}} \tag{4.6}$$

which can be illustrated by combining Equations (4.5) and (4.6) to get

$$\frac{d^2y}{dx_i^2} = \frac{\frac{y_{i+1}-y_i}{x_{i+1}-x_i} - \frac{y_i-y_{i-1}}{x_i-x_{i-1}}}{\frac{y_{i+1}-y_{i-1}}{x_{i+1}-x_{i_1}}} \tag{4.7}$$

Applying the curvature calculation to the major hysteresis loop in the previous figures results in the curvature response seen in Figure 4.2. The curvature value increases as it approaches the bends in the hysteresis loop, as expected. Each point on

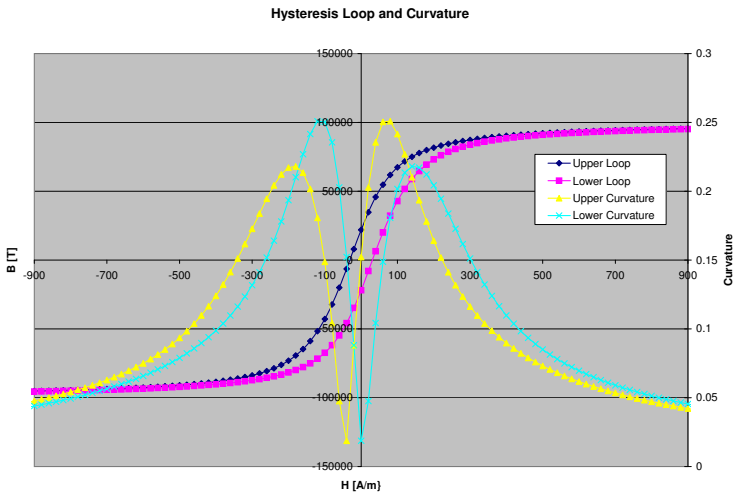

Figure 4.2: Plot of the calculated curvature of the hysteresis loops for both the upper and lower outer loops. The higher values can be used to identify regions where increased linearization points have a greater impact.

the graph can be sorted by the curvature around that point, and linearized only around the top n points in order to maximize effectiveness. The reduction in curvature through the linear portions of the hysteresis curve will prevent linearization around those points, although presently the algorithm does not necessarily select a particular point in the linear regions around which to approximate.

The results of the curvature-based linearization appear in Figure 4.3 for 10, 20, and 40-point approximations. As expected, fewer points are selected by the algorithm in the linear regions of the curve while the bends in the loop receive the majority of the attention. While potentially increasing the accuracy of the simulation by providing more slopes or permeabilities in the regions of higher curvature, when a restriction on the number of linearization points is enforced, corners of the curve can be missed as the algorithm reaches its limit of expansion points. This effect is most sharply seen in the 10-point approximation of Figure 4.3 (a), but is clearly seen in the 20-point figure

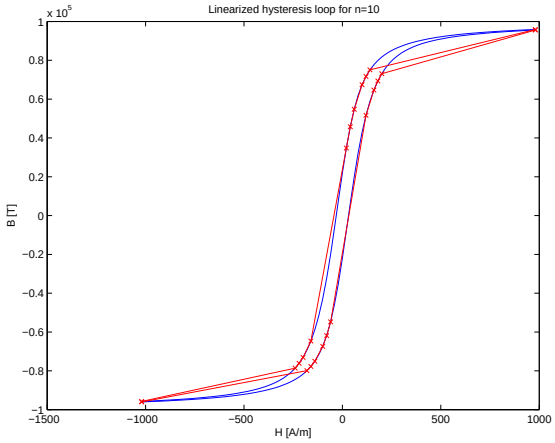

(a)

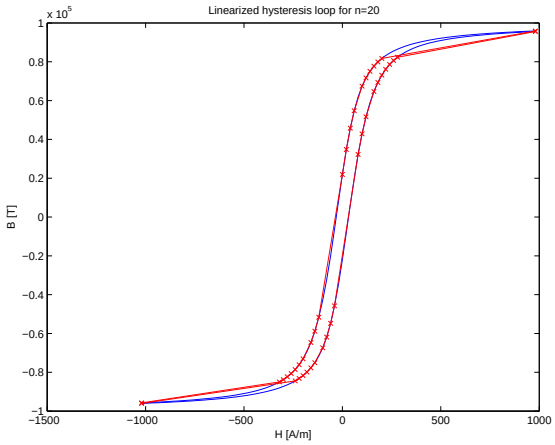

(b)

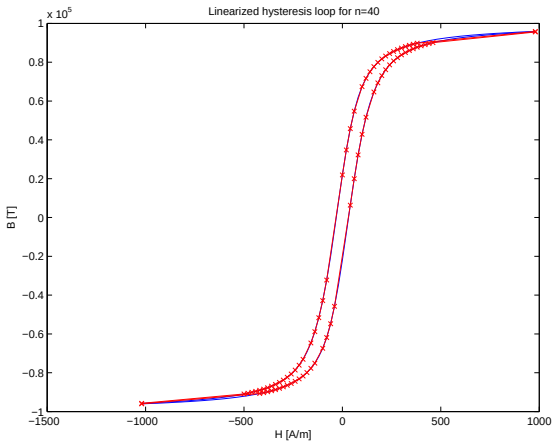

(c)

Figure 4.3: Linearized hysteresis curve using a curvature-based method for discretization up to 10 (a), 20 (b), and 40 (c) points per curve. Note that the number of points per curve represents each of the upper and lower portions of the hysteresis loop and does not include the end points.

Table 4.2: Summary of the average error between each point on the original and approximated hysteresis curves using a curvature-based linearization technique.

No. of points	Avg. Error (x10^5)[T/point]	Relative Performance (x10^5) [T]
n = 10	10.0	1.00
n = 20	5.84	1.16
n = 40	2.68	1.07

and first becomes less obvious with the 40-point approximation in Figure 4.3 (c).

To compare the curvature based method, we can apply the performance algorithm in the previous section and observe the results in Table 4.2. Surprisingly, the curvature method performed significantly worse than the fixed-width technique, most likely due to the chopping of the upper and lower regions around the bends in the loop. These long stretches of incongruencies would allow for the accumulation of significant error values according to the method's computations. This may indicate a shortcoming in the performance metric, depending on the application and its needs. Unlike the fixed-width method, the 10-point linearization produced the best overall performance, although the 40-point was a close second.

4.3 Curvature-Based, Minimum Width, Linearization

As seen in the previous section, selecting points for linearization based strictly on the curvature of the function can result in an approximation error in regions where the slope remains constant, but relatively large. This causes the tops of the knees in the curve to be cut off, producing significant error in the performance measurement. To reduce this error, a hybrid of the fixed-width and curvature methods may be used, whereby the curvature at each point is ranked and the highest point still taken, but with an enforced minimum distance between successive points. This prevents any linearization point from being too close to its neighbors to do any practical good and has the result of pushing the rest of the points farther up and down the curves on the

right and left sides, respectively.

The revised method produces the plots shown in Figure 4.4. Although the changes do not produce drastically different results from those in the original algorithm, the movement of the outer linearizations up and down the curves is noticeable and should produce a better rating for the overall method. The results of the performance metric appear in Table 4.3 and show an improvement for the 10-point approximation. The other two approximations performed worse, as corners of the bends were cut off in regions of large slope, resulting in high error norms in the performance computation.

Table 4.3: Summary of the average error between each point on the original and approximated hysteresis curves using a curvature-based linearization technique with an enforced minimum width between points.

No. of points	Avg. Error (x10^5)[T/point]	Relative Performance (x10^5) [T]
n = 10	8.72	0.87
n = 20	6.13	1.22
n = 40	3.22	1.29

Despite attempting to use a meaningful set of rules for choosing the linearization points, the fixed-width method managed to perform better than either of the curvature-based methods using the selected performance metric. A comparison of the overall performance results appears in Table 4.4. In fact, according to the performance metric, the fixed-width method performed considerably better than either of the curvature methods for all sets of approximations. A limitation of the performance method may be partly responsible, as the method rewards closer proximity to the original curve but ignores the discrepancy in slope between the graphs at each point. While the point positions affect the slopes at each point, they do so in an indirect way which may treat the methods unfairly if the curvature based methods match slope better at the expense of slightly mispositioned points.

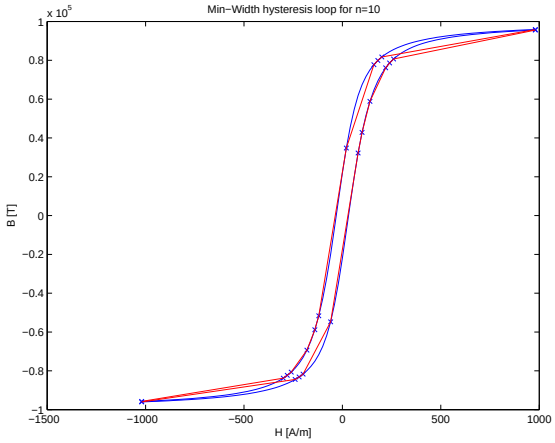

(a)

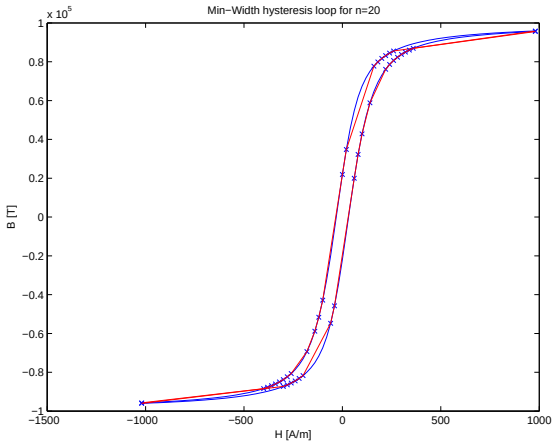

(b)

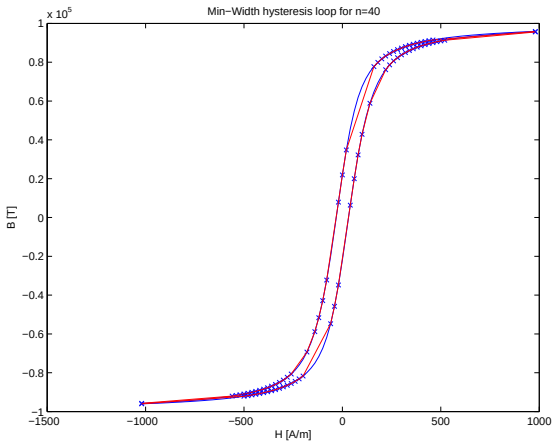

(c)

Figure 4.4: Linearized hysteresis curve using a curvature-based method with an enforced minimum distance between points for discretization up to 10 (a), 20 (b), and 40 (c) points per curve. Note that the number of points per curve represents each of the upper and lower portions of the hysteresis loop and does not include the end points.

Table 4.4: Comparison of the performance between the fixed width (1), curvature based (2), and min-width (3) methods for the selected approximations. In all cases, the fixed width method performed better than the curvature-based techniques.

Points	Method	Relative Performance (x10^5) [T]
n = 10	1	0.44
	2	1.00
	3	0.87
n = 20	1	0.22
	2	1.16
	3	1.22
n = 40	1	0.11
	2	1.07
	3	1.29

4.4 Drawbacks to Linearization

While the above methods provide a method for linearizing the major hysteresis loop for use in the reduction of the state-space system into a set of linearized reduced-order models, the methods make the incorporation of minor loops cumbersome. Linearization of the major loop and select minor loops could quickly increase the number of models necessary for capturing the entire hysteresis effects and without any guarantees of accuracy. For a time-domain simulation, a look-up table would require knowledge of both the present and past values of the input as well as the rate of change of the input in order to fully describe the nonlinear phenomena. Although the hysteresis models incorporate these parameters, look-up tables with all of this information would be tremendously cumbersome, requiring a better method for selecting the permeability for the reluctance network.

A practical solution would involve some method of model "training" in which linearization and subsequent reduction of the model is only done as needed [29]. The complete hysteresis model can be used to identify the precise permeability at any given point and determine if the model needs to be recalculated if the current value differs by a certain amount, say 10%. Each model can be stored and associated with a

permeability value instead of a set of input parameters, allowing the hysteresis model to handle the calculations of permeability. If the model identifies a permeability that has been previously saved, it can simply retrieve the model instead of reprocessing the flux-tube network. While potentially slower due to the processing of the models on-the-fly, once the simulation has been established, no loss in performance shold be discernible. It also promises equal or better efficiency than any preprocessing methods, since there is no possibility of processing model approximations that are never used. However, depending on the length of the simulation and the limits of the inputs, preprocessing may have its advantages, since it could result in more real-time results during the simulation if the major hysteresis loop is the only traversed path for saturation conditions.

CHAPTER 5

HYSTERESIS MODEL RESULTS

Including the hysteresis effects into the existing model requires several steps to track the input and model updates quickly and efficiently. Linearization techniques previously discussed can be incorporated to the extent of updating the permeability value when the present value deviates from the previous value by a certain percentage. For these results, 25% was used as the threshold at which the model was updated, with the exact value left at the discretion of the simulator. Decreasing the update threshold would, of course, increase the simulation accuracy. A major challenge to hysteresis simulation lies in the coupling between the current magnetization and past inputs. Because of this dependency, the simulation mechanism and the hysteresis model cannot be treated separately except in cases where the hysteresis model is completely linearized prior to simulation. However, this process has drawbacks in overhead and accuracy that are eliminated with real-time updating of the hysteresis model. To combine the two efforts, a complete simulation package has been proposed whereby both the hysteresis model and simulation are coupled with real-time data, allowing for the exchange and updating of model parameters and simulation outputs.

5.1 Simulation with Hysteresis

A flowchart of the model and simulation process appears in Figure 5.1. The main program consists of four major components sharing information in real time:

1. Hysteresis Model

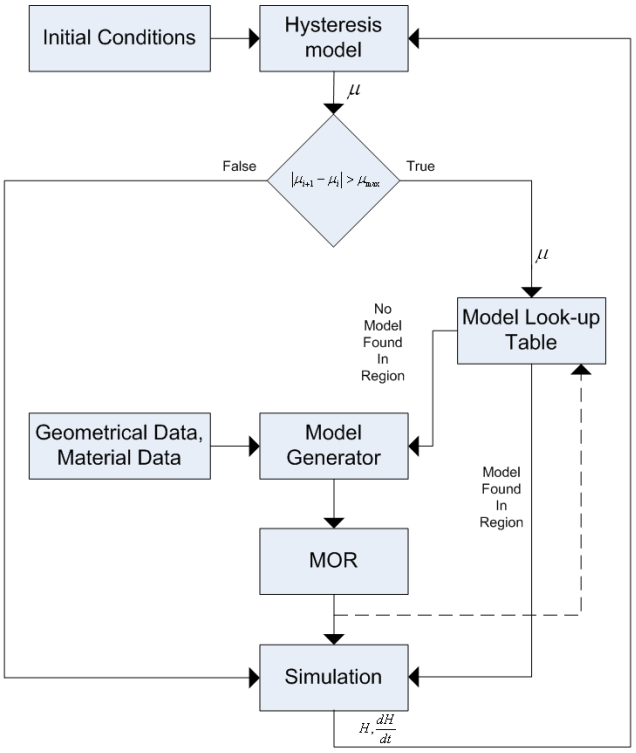

Figure 5.1: Flow chart of the proposed model and simulation method incorporating hysteresis.

2. Model Look-up Table

3. Model Generator

4. Simulation

The model-order reduction block is shown separate from the Model Generator to identify it as a unique process, but it performs a function that is essentially an extension of the model generation algorithm. The MOR and Model Look-up blocks are semiparallel tasks that share the same function: producing a reduced-order state-space model. If a model is not found in the table, the model generator processes a new model and stores it in the table in addition to sending it to the simulation block. The simulation block exchanges real-time information with the hysteresis model which determines the present permeability value and makes the decision on the accuracy of the model using the previous permeability. Results and discussion of the hysteresis, look-up table, and generator blocks are presented in their own section. The simulation block can be supplied by any mathematical package capable of handling numerical integration and matrix algebra.

5.1.1 Hysteresis model

The hysteresis model block is a placeholder for the simulator's model of choice. A major advantage to real-time updating of simulation results is the ability to drop virtually any hysteresis model into the block, regardless of the major mechanism behind the model. For instance, a Jiles-Atherton model computes the magnetization based on the present value of magnetic field and the sign of the rate of change in the field using a series of nonlinear differential equations. Both of these parameters are sent from the simulation block, allowing the model to be updated and the permeability extracted. In this case, differential permeability is used to prevent numerical errors around zero field intensity.

The Preisach model uses a completely different base theory for developing the hysteresis curve. Unlike the Jiles-Atherton, it is restricted to real-time simulation since the Preisach domain requires knowledge of past magnetic field inputs. Fortunately, the proposed program performs this function as a matter of practice, and for this reason, the Preisach model is used in the hysteresis model block for the sample simulation.

A 1 V, 60 Hz signal was applied to the simulated three-zone MEC model and can be referenced in Figure 5.3 (p. 54). Figure 5.2 shows the status of the hysteresis block 5 ms into the simulation in both the Preisach domain and the B-H curve. The Preisach domain reflects the monotonically increasing input up to roughly $t = 4.25$ ms just before the voltage crosses the x-axis. In this case, the voltage input is not large enough to cause any saturation effects, although the model handles such an input in the same manner. The return path on the vertical sweep can be seen near the right vertex of the limiting triangle, resulting from the change in sign of $\frac{dH}{dt}$. The hysteresis curve follows accordingly on the minor loop in Figure 5.2 (b). At the chosen snapshot in the simulation, the differential permeability can be calculated by taking the difference in the magnetization at the last and second-to-last points and dividing by the corresponding change in magnetic field.

Once the updated permeability is computed, the hysteresis model makes a decision based on the previous permeability value, shown externally in Figure 5.1. If the new μ value exceeds the prior value by a user-specified percentage, the hysteresis block passes program flow to the model generation portion of the simulation, jointly held by the look-up table and generator blocks. If the updated value falls within the specified range, the program flow remains with the hysteresis model and simulation blocks and the real-time simulation continues. This real-time update of the permeability solves the issue of linearization addressed in Chapter 4 while still minimizing the number of models required to compute.

The only additional information required by the hysteresis block is the necessary

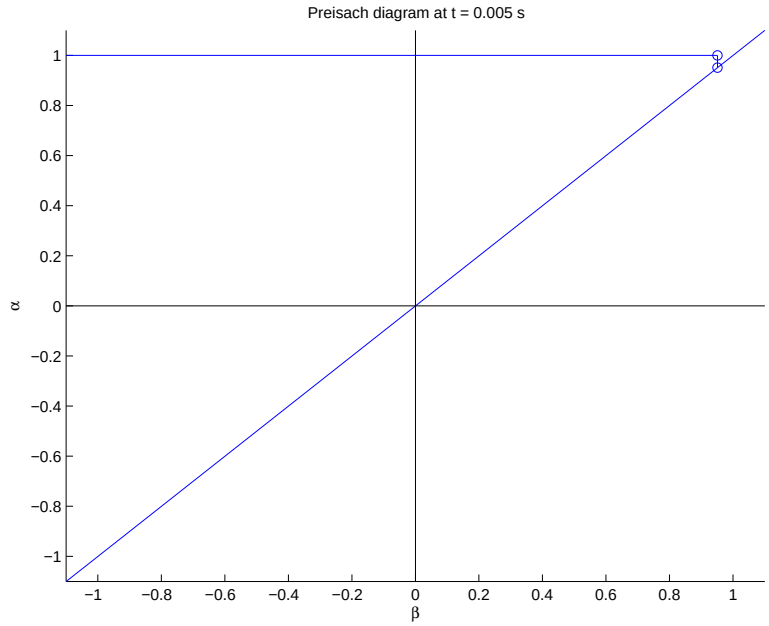

(a)

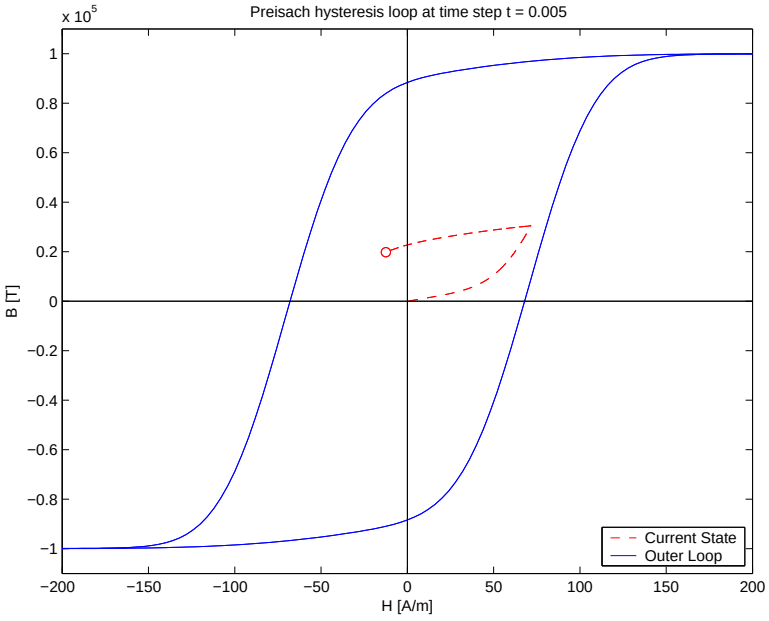

(b)

Figure 5.2: Preisach domain (a) and corresponding magnetization plot (b) at t = 0.005 s. The outer loop in (b) is shown for perspective.

initial conditions and material data for the device. In the case of the Preisach model, the initial magnetization state of the material is required to properly initiate the Preisach domain. Many other models do not require initial conditions, but the block is represented as a generic input to maintain compatibility with any model as well as capture the material data which all models require for accuracy. If the device is known to operate within a certain region, direct B-H characteristics may be measured and dropped into the block as well. A simple look-up function can match the simulation's H and $\frac{dH}{dt}$ values to the appropriate curve (ascending or descending) and region of operation. The next differential permeability can then be calculated and the program flow continued normally. While this method only works if the device is operated in the region where data exists, it is possible to extrapolate a limited data set to a theoretical model [30], [31]. This process illustrates the flexibility and extensibility of the proposed model for practical purposes.

5.1.2 Model look-up

Once the hysteresis model block has determined that an updated model is necessary, the look-up table accepts the newly calculated permeability and searches for recorded values with upper and lower limits that include the new μ. This prevents the program from duplicating the effort required to process a new model, reducing computational overhead and speeding up the simulation. If a suitable range of permeabilities is not located, the block passes control the model generator and only then is a new model created. The net effect is a sluggish startup as each new permeability requires an additional model and an eventually noticeable performance increase as updated permeabilities and their associated models are found in the table.

Table 5.1 shows the stored permeabilities and their models 5 ms into the simulation. A total of 19 models are listed since the start of the simulation, allowing for up to a

25% percent change in μ. While this may seem like a significant amount of data for such a short time period, the total number of processed data points in that time period exceeds 2000, representing a 99% decrease in potential model generation. Additionally, the table presented here overestimates the number of generated models, as all model updates mandated by the hysteresis block are included. Updates marked with an asterisk, although required, represent permeability values that fall into previously generated ranges. Thus, they do not require updating and can simply be pulled from the table. This method is particularly useful when minor loops are involved, since separately predicting each loop trajectory and its linearization would be nearly impossible. Instead, for all practical purposes, the minor loops can be neglected as long as their resulting permeabilities are known.

5.1.3 Model generation

If no suitable permeability is found in the look-up table, the program moves to the model generator block to process a new model around the updated μ value. This involves the creation of a new state-space matrix from scratch and, thus, limiting the number of calls to this routine can be a major concern for simulation performance, depending on the desired level of detail in the model.

The model generator interacts with the largest number of subsystems as it coordinates several tasks throughout the simulation. Initially, geometry and material data must be gathered through any means necessary. From a simple 2-D model to a complex, 3-D CAD generation system, the model generator breaks the geometry and material data into a flux tube and grid system, as appropriate, similar to the processes used in finite-element analysis methods. Fortunately, once the geometry and material parameters have been established, the model can isolate the purely constant, geometric terms, as discussed in Chapter 4. Isolating the constant terms in $\mathbf{A}$ allows the updates

Table 5.1: Contents of the look-up table for t = 0.005 s and model-order = 3. Values with asterisk indicate models whose permeabilities overlap by the 25% margin and would not be recalculated according to the algorithm.

Index	μ_r	H(s)
1	80.43	$\frac{4.96E+10s^2+9.25E+24s+2.20E+38}{s^3+2.02E+14s^2+6.87E+27s+5.06E+36}$
2	114.32	$\frac{4.38E+04s^2+7.23E+12s+1.52E+20}{s^3+1.79E+08s^2+5.37E+15s+3.50E+18}$
3	143.59	$\frac{3.49E+04s^2+4.58E+12s+7.68E+19}{s^3+1.42E+08s^2+3.40E+15s+1.77E+18}$
4	180.65	$\frac{2.77E+04s^2+2.90E+12s+3.86E+19}{s^3+1.13E+08s^2+2.15E+15s+8.87E+17}$
5	227.15	$\frac{2.21E+04s^2+1.83E+12s+1.94E+19}{s^3+9.00E+07s^2+1.36E+15s+4.46E+17}$
6	284.28	$\frac{1.76E+04s^2+1.17E+12s+9.89E+18}{s^3+7.20E+07s^2+8.69E+14s+2.28E+17}$
7	355.39	$\frac{1.41E+04s^2+7.48E+11s+5.06E+18}{s^3+5.76E+07s^2+5.56E+14s+1.16E+17}$
8	445.99	$\frac{1.12E+04s^2+4.75E+11s+2.56E+18}{s^3+4.59E+07s^2+3.53E+14s+5.89E+16}$
9	557.72	$\frac{8.98E+03s^2+3.04E+11s+1.31E+18}{s^3+3.67E+07s^2+2.26E+14s+3.01E+16}$
10	699.29	$\frac{7.16E+03s^2+1.93E+11s+6.65E+17}{s^3+2.93E+07s^2+1.44E+14s+1.53E+16}$
11	875.38	$\frac{5.72E+03s^2+1.23E+11s+3.39E+17}{s^3+2.34E+07s^2+9.16E+13s+7.79E+15}$
12	1094.7	$\frac{4.58E+03s^2+7.88E+10s+1.73E+17}{s^3+1.87E+07s^2+5.86E+13s+3.98E+15}$
13*	67.569	$\frac{7.41E+04s^2+2.07E+13s+7.37E+20}{s^3+3.03E+08s^2+1.54E+16s+1.69E+19}$
14*	84.531	$\frac{5.93E+04s^2+1.32E+13s+3.76E+20}{s^3+2.42E+08s^2+9.82E+15s+8.65E+18}$
15*	105.67	$\frac{4.74E+04s^2+8.46E+12s+1.93E+20}{s^3+1.94E+08s^2+6.29E+15s+4.43E+18}$
16*	132.2	$\frac{3.79E+04s^2+5.41E+12s+9.84E+19}{s^3+1.55E+08s^2+4.02E+15s+2.26E+18}$
17*	165.56	$\frac{3.03E+04s^2+3.45E+12s+5.01E+19}{s^3+1.24E+08s^2+2.56E+15s+1.15E+18}$
18*	207.32	$\frac{2.42E+04s^2+2.20E+12s+2.55E+19}{s^3+9.87E+07s^2+1.63E+15s+5.87E+17}$
19*	259.27	$\frac{1.93E+04s^2+1.41E+12s+1.30E+19}{s^3+7.89E+07s^2+1.04E+15s+3.00E+17}$

in permeability to be handled by a simple scalar multiplication, improving the efficiency of the model generation. Simulations of machines and any other motion can complicate this process or prevent it entirely, reducing the performance to the original geometric update in the worst case.

Once the state-space system has been updated with the new permeability, the model generator passes control to the model-order reduction technique of choice. This process is identified separately in Figure 5.1, but could easily be incorporated as part of the same procedure. The MOR algorithm remains unaffected by any of the model generation methods or the incorporation of hysteresis, an additional benefit in the transition to hysteresis simulation. Once the reduced-order model is completed, it can be sent to the simulation block for the next time-step update with the new dynamics. A copy of the system is also stored in the look-up table for future use, if necessary.

5.2 Summary of Simulation Results

Each component of the proposed model was measured in some manner for a three-zone magnetic equivalent circuit model including hysteresis. A 1 V, 60 Hz sine wave was applied to the network circuit and the input voltage and magnetic intensity field measured with the plots appearing in Figure 5.3. The magnetic field waveform is proportional to the input current and thus provides an indicator of the input-output relationship. It matches the waveform expected for a simple RL circuit as exponential charging is clearly visible in the first half of the plot.

The hysteresis model performed as expected and, although no saturation took place, the effects of minor loops and reversal points were adequately captured. Model generation used the previously identified algorithm from Chapter 3 and was not reduced due to the already oversimplified approximation enforced. However, a finer grid could easily have been used and any number of model-order reduction techniques

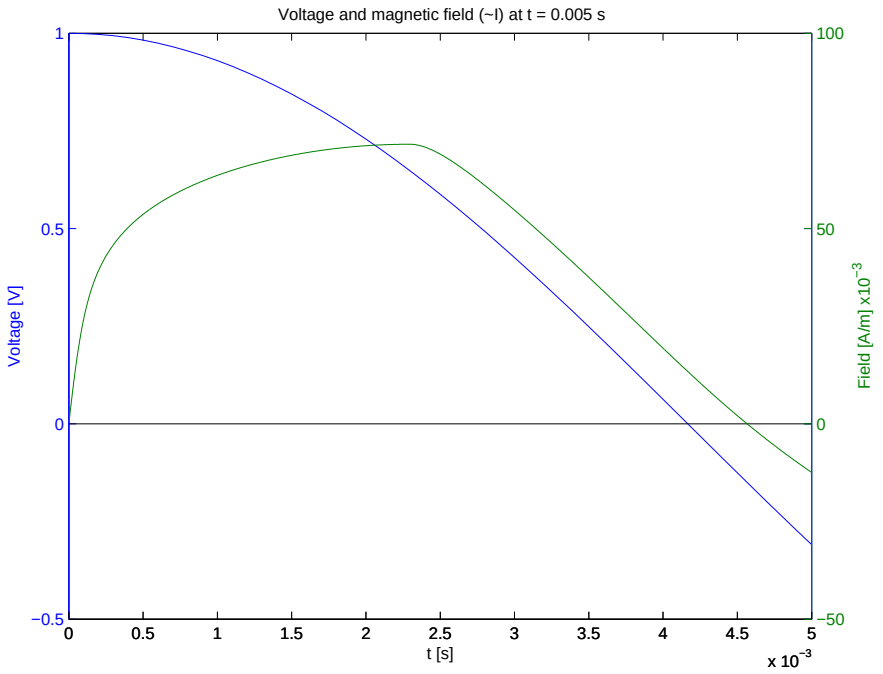

Figure 5.3: Plot showing the input voltage (sinusoid) and the magnetic field up to t = 0.005 s.

employed to illustrate their inclusion in the process. The model look-up table dramatically reduced the number of calls to the model generation algorithm from a possible 2000 to only 19. Increasing the time limits on the simulation would increase this effectiveness as more previously stored models are selected from the look-up table.

CHAPTER 6

VALIDATION OF UNIFORM PERMEABILITY

The previous chapter developed a process for simulating hysteresis under the assumption of constant permeability across the device. The hysteresis model accounts for the first order effect of changes in the permeability by updating the value as the applied field moves up or down the hysteresis curve, but does not account for any differences in permeability between individual flux tubes. Whether or not the variation in permeability presents a second order effect or greater is the subject of this chapter.

6.1 Iterative Solutions for Permeability

We begin with the revised flux tube circuit model shown in Figure 6.1. Each of the reluctances can be modeled as variable resistors in the magnetic domain with their resistance depending in part upon the amount of flux passing through them, according to Maxwell's equations and the magnetic constitutive relation,

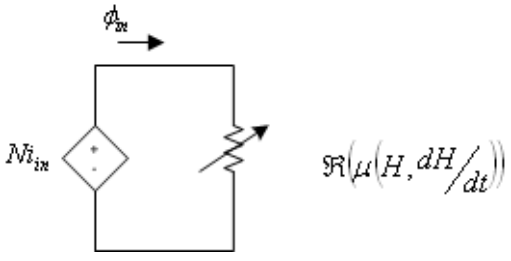

Figure 6.1: Modified reluctance term illustrating the variation in permeability as a function of applied field.

$$\int\int_S \mathbf{B} \cdot d\mathbf{S} = \phi \tag{6.1}$$

$$\mathbf{B} = \mu \mathbf{H} \tag{6.2}$$

The reluctance values, of course, affect the amount of magnetic flux propagating through the flux tubes, creating an interdependence that requires an iterative process to solve until convergence. As an example, consider the plot in Figure 6.2. It is assumed that the material begins from a negative saturation state with zero input voltage to the circuit, resulting in a permeability of μ_{-sat} and corresponding reluctance, $\mathcal{R}_{-sat}$. Application of an input voltage causes current to flow in the electrical circuit, inducing a magnetic flux corresponding to

$$\phi = \frac{Ni}{\mathcal{R}_{-sat}}$$

which is accurate if and only if the voltage input is sufficient to put the device into the negatively saturated state. If not, then the permeability is at one of its smallest possible values and overestimates the reluctance, making the flux appear smaller than its actual value. We know from Equations (6.1) and (6.2) that flux is proportional to the magnetic field intensity, H, making this quantity underestimated as well. Underestimation of the field intensity moves the next iterative operating point towards the center of the B-H curve, μ_1 in the figure, for a positive voltage input as an example. This new operating point has an increased permeability, almost at the maximum for the example case, and lowers reluctance to allow more flux through the circuit. This increased flux has a proportional effect on field intensity, driving the next operating point further up the curve to μ_2. The new point produces an increased reluctance, driving the flux down and moving the operating point along the curve to a point of slightly higher permeability, and so on until the iterations converge on the

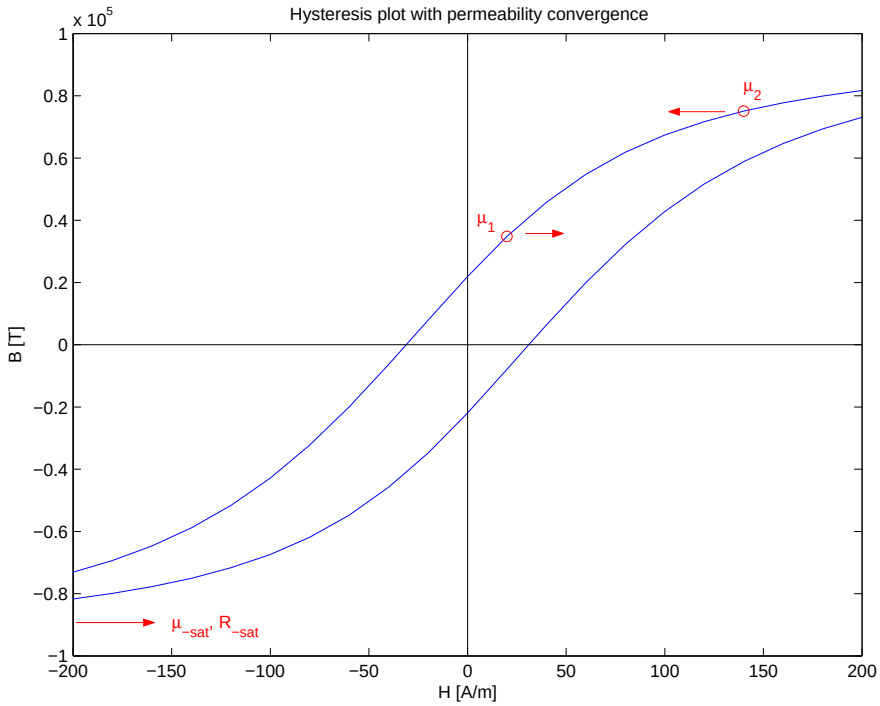

Figure 6.2: Plot showing the convergence of an iterative solution for finding permeability from the hysteresis plot.

equilibrium value.

The process for identifying the equilibrium flux tube permeability is relatively straightforward, requiring only a few iterations and stabilized by the monotonically increasing properties of both the upper and lower hysteresis curves. Handling a decreasing field intensity works in the exact same manner as an increasing input but on the lower curve instead of the upper. In the event of minor loops caused by reversal points below saturation, the hysteresis model needs to be updated to provide the new B-H points used in the process, which may require some speculation about where the next reversal point lies. However, once the initial convergence is reached, the difference in the sequence of permeabilities should be close to continuous for any input that has no discontinuities. For the purpose of simulation, the only permeability necessitating any significant number of iterations should be the initial equilibrium input taking the function from negative saturation to its initial value. The succeeding

permeabilities then lie within a reasonable margin from each other, again, provided that the input is close to continuous.

6.2 Geometric Effects on the Reluctance Network

Once the sequence of permeability is established for a flux tube, the following solutions become relatively simple due to only minor changes from one time step to the next. However, a system of flux tubes provides a more interesting result, as changes in geometry between neighboring tubes can produce different permeabilities for the same steady-state input to the device. Consider the extension of the circuit in Figure 6.1 to include more reluctances in parallel with the first. Excluding eddy currents and their resulting inductive elements, the circuit can still be simplified to an equivalent reluctance and solved in the same manner as in the previous section. However, the direct solution of the equivalent circuit obscures the individual reluctances from the solution when they are lumped into one reluctance.

The discussion in Chapter 4 opened with the separation of the system matrix into a purely geometrical component and the same concept can be used here to identify a new matrix with all of the individual flux tube reluctances, with the exception that none of the values are lumped into equivalent reluctances. Figure 6.3 shows the matrix with the reluctance of each flux tube with fixed permeability across the device. The matrix indexes correspond to the position of the flux tube in the device cross section, and because of the device geometry of the toroid, the only variation in reluctance appears in the radial direction.

For the case of fixed cross-sectional permeability, the variation in reluctances lies between 3.1×10^5 and 0.2×10^5 amp-turns per weber with a standard deviation of 0.87×10^5 and an average of 1.7×10^5. Table 6.1 organizes these results for comparison to differential permeability statistics from the next section. Differential permeability is

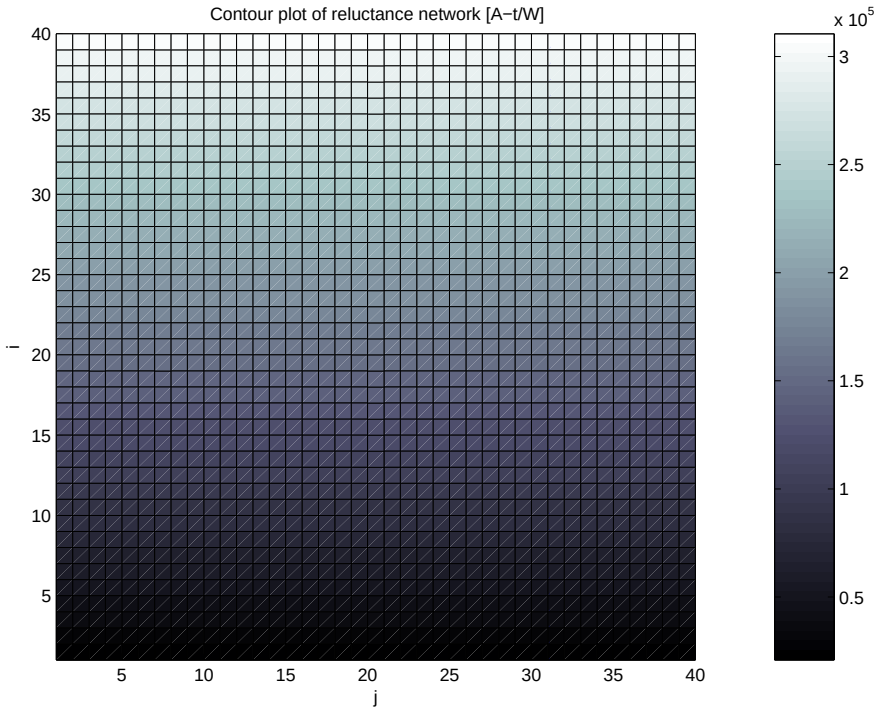

Figure 6.3: Surface plot showing the distribution of reluctances for a network of flux tubes in a toroidal core for flux tube indexes, i and j.

used here to prevent complications from undefined values around the origin.

Approximation of constant permeability throughout the device cross section might be tolerable for most simulations as the reluctances are relatively close around the mean.

6.3 Cross-Sectional Permeability Distribution and Variance

Like the reluctance distribution, the variation in permeability can be identified through the cross section of the device. Such a variation is expected since the geometric variation in the flux tubes will produce different reluctances and, hence, different fluxes through each individual tube. This variation in flux should force the permeabilities to different operating points on the B-H curve. In principle, the permeabilities should act as a compensating mechanism to drive the reluctances

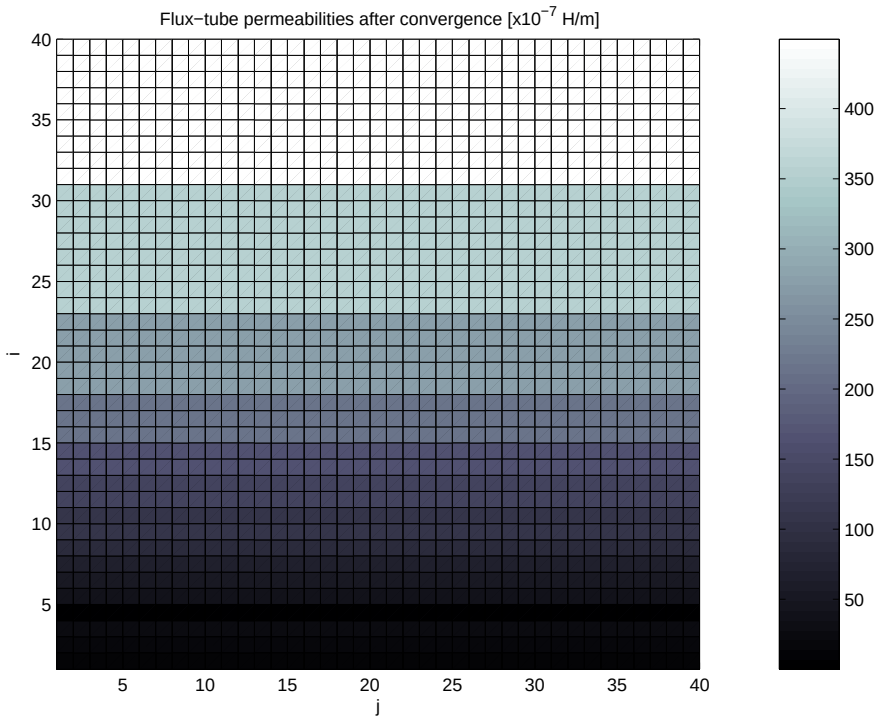

Figure 6.4: Surface plot showing distribution of permeability values throughout the cross section of a toroidal core with flux tube indexes, *i* and *j*.

toward each other in order to more closely match the fluxes through the tubes. The surface plot in Figure 6.4 shows the distribution of the permeabilities. The results in Table 6.1 show a standard deviation of 12.44 and an average of 15.2, slightly more scattered than the reluctances.

An interesting property of the distribution in Figure 6.4 is the more discretized nature of the values compared to those of the reluctances in Figure 6.3. The discrepancy between the continuity in the reluctances and corresponding permeabilities for the same device geometry can be attributed to the discrete nature of the hysteresis curve used to identify the differential permeabilities. In this case, the reluctance values were calculated using continuous values over the the device geometry and then discretized over the flux tube network. So, although the flux tubes can be separated into individual components, their reluctances in the radial direction are unique products of their geometry. The permeabilities, however, are restricted to

Table 6.1: Comparison of the statistical properties of the reluctance and permeability variations over the toroidal cross section.

Data	σ	$\bar{\mu}$	Min.	Max.
Reluctance (Fixed μ)	$0.87\text{x}10^5$	$1.7\text{x}10^5$	$0.2\text{x}10^5$	$3.1\text{x}10^5$
Permeability	12.44	15.2	0.16	41.4
Reluctance (Variable μ)	$4.9\text{x}10^5$	$11.4\text{x}10^5$	$3.2\text{x}10^5$	$2.0\text{x}10^6$

the regions of the hysteresis curve where data is available. Many of the individual flux tubes fall into the same regions of magnetic field intensity on the hysteresis curve between available data points.

As a comparison, the results of the reluctance distribution with variable permeability are also listed in Table 6.1. The distribution shows roughly the same variance as the reluctance with fixed permeability, but at slightly higher values. The hypothesis on page 59 indicated that the reluctance variation should improve as the permeability values were allowed to change, compensating up or down for restrictions in flux as necessary. This clearly is not the case in Table 6.1 and the applied input and associated operating point may need to be considered to reconcile the differences.

Figure 6.5 shows individual flux tube permeabilities' associated B-H characteristics overlaid on the hysteresis loop to identify their operating points on the curve. This particular input voltage has pushed the flux tubes to the point of saturation on the B-H curve, causing a much wider variation in permeability than would be achieved in the linear operating region. The fixed-permeability reluctance values were taken for nominal input in the linear region, resulting in only geometric variation between the reluctances and much lower reluctance values. Pushing the device to near saturation produces higher reluctances, as expected, and contributes differing permeability values to the statistical variance.

The resulting flux distribution within the device appears in Figure 6.6. The distribution produces a more interesting result as the permeability and geometry of the flux tubes combine to keep the overall flux through the device as constant and high as

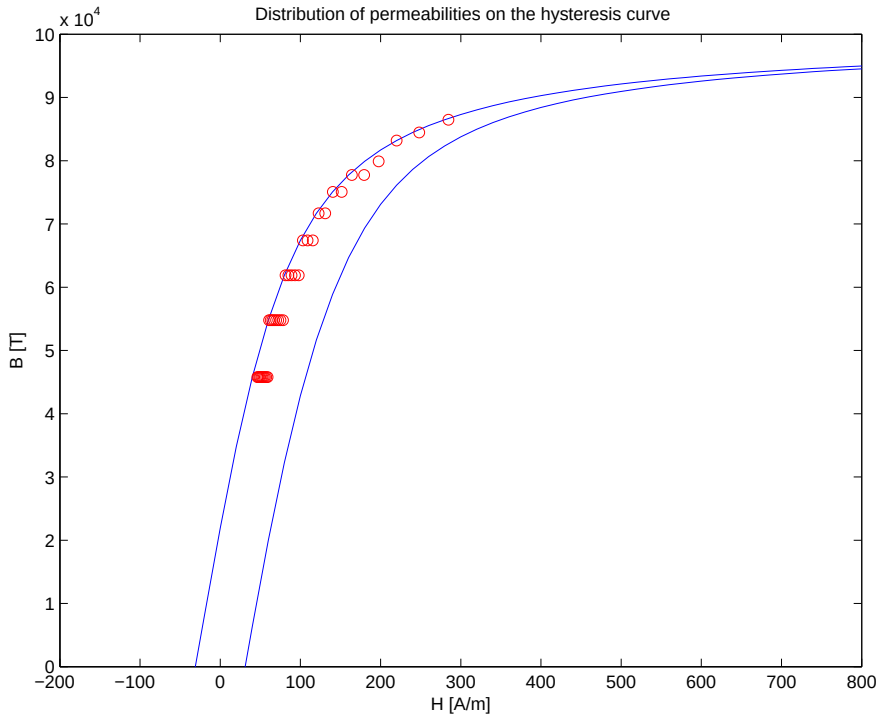

Figure 6.5: Plot of a major hysteresis curve with the distribution of B-H steady-state operation points overlaid for each flux tube.

possible. The regions of constant permeability are clearly visible as their fixed values across the region prevent the flux from getting as high as possible in other parts of the region. For instance, rows 40 through 32 show a region of reluctances where the permeability remains fixed due to the discretized nature of the hysteresis plot. The permeability is fixed as high as possible for the region, making the reluctance as low as possible to increase the flux. The geometrical components then take effect across the region, producing higher reluctances as the distance from the center is increased. This process repeats for each region, resulting in the same pattern and nearly the same values for flux in the entire device. The only variation to the pattern occurs in the inner region where the geometry produces such naturally low reluctances that the permeability value is forced into the saturation regions of the hysteresis curve. The smaller geometrical reluctance contributions produce the opposite effect – driving flux down – since the permeability decreases sharply in the saturation region.

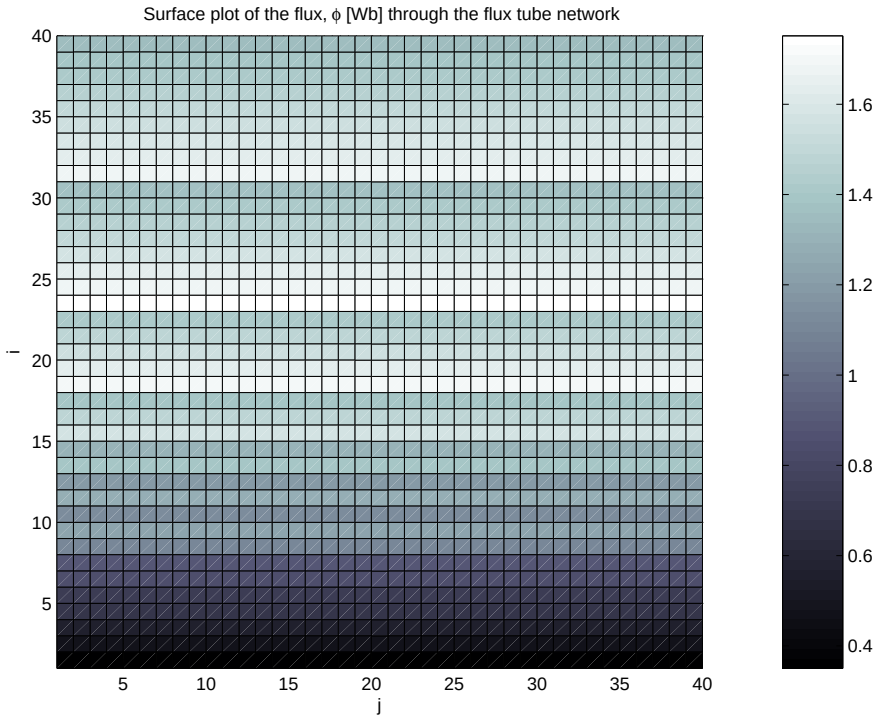

Figure 6.6: Surface plot of the distribution of flux within the flux tube network.

6.4 Summary

The assumption of uniform permeability in a device is certainly not accurate from a physical perspective, as demonstrated in this chapter. Variation in permeability as magnetic field intensity changes is an important effect to capture and can be done with a single calculation to a first-order effect. The convergence to an equilibrium value can likely be ignored as long as the initial value is approximately correct for the first applied input. Any subsequent values for continuous input should produce very close results without requiring any iterative solving and thus, only step changes in the input pose any concern. Starting with zero initial conditions provides a practical and easy manner to ensure simulation accuracy.

Differences in flux tube geometry produce a second source of variations in reluctance. Fortunately, these contributions are typically fixed with the exception of regions of mechanical motion, but that topic is left for future work. As a result of fixed

geometry, the effect is easily incorporated into the model generator and needs processing only once on startup. The effects of geometry acting in concert with permeability variations produce an effect that drives the flux towards the more constant cross-sectional values that were assumed in Chapter 4. This physical effect reduces the accuracy of the model under constant assumptions, since constant permeability produces a variation in flux consistent with geometrical variations, while adding variable permeabilities actually smooths out the flux distribution in the device. In regions of saturation, the permeabilities will experience a smaller variation, and the model becomes equivalent to the constant permeability model in the upper limits of the input magnitude. However, in the linear region this phenomenon may play an important role in simulation results.

CHAPTER 7

CONCLUSION

Because of the challenges associated with the incorporation of nonlinear effects, a practical and usable solution must be available to quickly model machines and other magnetic devices while maintaining a desired level of accuracy. However, before a serious discussion of simulation methods can take place, appropriate models must be identified to capture the hysteresis effects. Chapter 2 outlined some of the current models presented in recent literature and focused on the development of two of the most popular models. Despite their derivation from basic magnetic principles, the models rely on drastically different methods for implementation, requiring careful analysis when selecting one for simulation. Chapter 2 discussed some of the trade-offs between the models for use in the proposed simulation program.

Further background information was covered in Chapter 3 to provide a basis for the linear analysis methods with eddy current included. The introduction of flux tubes as magnetic network elements and modeling methods produced in [8] were rederived for use in later analysis. Application of model-order reduction techniques to the magnetic network state-space systems was presented as well, with special focus on the assumption of constant permeability throughout the device cross section.

With the establishment of the linear state-space system and nonlinear hysteresis models, a discussion of possible approaches to the integration of both concepts was developed in Chapter 4. The suggested methods focused on the linearization of the major hysteresis loop and subsequent recalculation of the MEC reduced-order models. Multiple linearization techniques were compared to provide the closest approximation

to the hysteresis loop, and although curvature methods were presented based on changing slope, a fixed-width method proved to be the best approximation according to the chosen performance metric. The chapter concluded with the suggestion of an alternative concept, requiring the real-time hysteresis model development and corresponding permeability measurement.

Chapter 5 proposed a simulation program flow to incorporate the real-time hysteresis measurements with simulation outputs while maximizing efficiency. The concepts of MEC reduced-order modeling were utilized in a model generation system and the results were saved and indexed for possible future use. A system was developed to cross-check the present and past permeability values to maintain model accuracy to a desired level while capitalizing on previously computed models to save on processing overhead. Significant achievement was made in the reduction of the number of necessary models for a given number of simulation points, although the assumption of fixed cross-sectional permeability was still enforced.

The assumption of constant cross-sectional permeability was addressed in Chapter 6 in addition to the appropriateness of single-iteration permeability values. It was shown that, without regard for initial conditions, the permeability of the flux tubes may not be solved accurately in a single computation. However, with attention to the initial input and correlation to the starting permeability, iterative solutions to permeability may not be necessary. The cross-sectional variance in permeability and reluctance was illustrated and determined to be a potential factor in MEC simulation results. Corrective methods require the dc magnetic simulation and permeability measurement of the circuit for the fixed input value.

Providing engineers with modeling and simulation tools that fill the gap between computationally intense finite-element analysis and accuracy-challenged analytical solutions will be an important part in the design of next generation magnetic devices, particularly electrical machines. Further investigation into model-order reduction with

hysteresis will require the extrapolation of the techniques in this thesis to 3-D magnetic devices and the inclusion of force analysis. Large gains in advancing MEC methods to the level of FEA in terms of design and model automation have already been made, and this thesis and future work will serve to polish the modeling techniques for greater gains in accuracy and performance.

REFERENCES

[1] L. Qu and P. Chapman, "Toward a system for automatic extraction of low-order models for magnetic devices," in *IEEE Workshops on Computers in Power Electronics*, 2006, pp. 193–198.

[2] L. Qu and P. Chapman, "Extraction of low-order non-linear inductor models from a high-order physics-based representation," *IEEE Transactions on Power Electronics*, vol. 21, pp. 813–817, 2006.

[3] L. Qu and P. Chapman, "Extraction of dynamic, low-order models for magnetic devices based on finite element analysis with hysteresis," in *Power Electronics Specialists Conference*, 2007, pp. 2082–2088.

[4] L. Qu and P. Chapman, "Extraction of dynamic low-order nonlinear inductor models based on steady state solutions," in *Power Electronics Specialist Conference*, 2006, pp. 1–9.

[5] M. Amrhein, "Induction machine performance improvements - design-oriented approaches," Ph.D. dissertation, University of Illinois at Urbana-Champaign, 2007.

[6] J. Perho, "Reluctance network for analysing induction machines," Ph.D. dissertation, Helsinki University of Technology, 2002.

[7] C. Rasmussen and E. Ritchie, "A magnetic equivalent circuit approach for predicting pm motor performance," in *Rec. Industry Applications Conference*, 1997, pp. 10–17.

[8] A. Davoudi and P. L. Chapman, "Eddy current modeling with order-reduction in magnetic equivalent circuits," in *IEEE Power Electronics Specialists Conference*, June 2007, pp. 2069–2074.

[9] M. Takach and P. Lauritzen, "Survey of magnetic core models," in *Applied Power Electronics Conference and Exposition*, vol. 2, 1995, pp. 560–566.

[10] I. Mayergoyz, *Mathematical Models of Hysteresis*. New York, NY: Springer-Verlag, 1991.

[11] O. Alejos and E. Torre, "Improving numerical simulations of Preisach models for accuracy and speed," *IEEE Transactions on Magnetics*, vol. 36, 5 part 1, pp. 3102–3104, 2000.

[12] E. Cardelli, E. D. Torre, and B. Tellini, "Direct and inverse Preisach modeling of soft materials," *IEEE Transactions on Magnetics*, vol. 36, no. 4, pp. 1267–1271, July 2000.

[13] S. Naidu, "Simulation of the hysteresis phenomenon using Preisach's theory," in *IEE Proceedings*, vol. 137, no. 2, March 1990, pp. 73–79.

[14] P. Nakmahachalasint, K. D. Ngo, and L. Vu-Quoc, "A behavioral model for frequency-dependent hysteresis in power ferrites," *IEEE Transactions on Magnetics*, vol. 40, no. 4, pp. 1784–1790, July 2004.

[15] I. Mayergoyz and G. Friedman, "Isotropic vector Preisach model of hysteresis," *Journal of Applied Physics*, vol. 61, p. 4022, 1987.

[16] D. Jiles and J. Atherton, "Theory of ferromagnetic hysteresis," *Journal of Magnetism and Magnetic Material*, vol. 61, pp. 48–60, 1986.

[17] N. Sadowski, N. Batistela, J. Bastos, and M. Lajoie-Mazenc, "An inverse Jiles-Atherton model to take into account hysteresis in time-stepping finite-element calculations," *IEEE Transactions on Magnetics*, vol. 38, pp. 797–800, 2002.

[18] P. L. Chapman and S. D. Sudhoff, "Dynamic lossy inductor model for power converter simulation," *Applied Power Electronics Conference and Exposition*, vol. 1, pp. 137–143, March 2002.

[19] D. Lederer, H. Igarashi, A. Kost, and T. Honma, "On the parameter identification and application of the Jiles-Atherton hysteresis model for numerical modelling of measured characteristics," *IEEE Transactions on Magnetics*, vol. 35, no. 3, pp. 1211–1213, May 1999.

[20] J. Izydorczyk, "A new algorithm for extraction of parameters of Jiles and Atherton hysteresis model," *IEEE Transactions on Magnetics*, vol. 42, no. 10, pp. 3132–3134, October 2006.

[21] D. Jiles, J. Theolke, and M. Devine, "Numerical determination of hysteresis parameters for the modeling of magnetic properties using the theory of ferromagnetic hysteresis," *IEEE Transactions on Magnetics*, vol. 28, pp. 27–35, 1992.

[22] A. Bergqvist, "A simple vector generalization of the Jiles-Atherton model of hysteresis," *IEEE Transactions on Magnetics*, vol. 32, 5 part 1, pp. 4213–4215, 1996.

[23] J. Leite, N. Sadowski, P. Kuo-Peng, N. Batistela, J. Bastos, and A. de Espindola, "Inverse Jiles-Atherton vector hysteresis model," *IEEE Transactions on Magnetics*, vol. 40, 4 part 1, pp. 1769–1775, 2004.

[24] A. Davoudi and P. L. Chapman, "A general framework for automated physics-based reduced-order modeling of electromechanical systems," in *Proceedings of the 2007 Summer Computer Simulation Conference*, 2007, pp. 221–228.

[25] A. Davoudi, L. Qu, and P. L. Chapman, "Summary of recent work on reduction techniques applied to electromechanical modeling," in *IEEE Electric Ship Technologies Symposium*, May 2007, pp. 363–370.

[26] R. Barrett et al., *Templates for the Solution of Linear Systems*. Philadelphia, PA: SIAM, 1994.

[27] R. Freund, G. Golub, and N. Nachtigal, "Iterative solutions of linear systems," *Acta Numerica*, vol. 1, pp. 57–100, 1992.

[28] Y. Saad, *Iterative Methods for Sparse Linear Systems*, 2nd ed. Philadelphia, PA: SIAM, 2003.

[29] M. Rewienski and J. White, "A trajectory piecewise-linear approach to model order reduction and fast simulation of nonlinear circuits and micromachined devices," *IEEE Transactions on Computer-Aided Design*, vol. 22, 2, pp. 155–170, 2003.

[30] D. C. Aliprantis, S. D. Sudhoff, and B. T. Kuhn, "A brushless exciter model incorporating multiple rectifier modes and Preisach's hysteresis theory," *IEEE Transactions on Energy Conversion*, vol. 21, no. 1, pp. 136–147, March 2006.

[31] S.-T. Liu, S.-R. Huang, H.-W. Chen, and T.-Y. Hsien, "Current transformer module basing the Jiles-Atherton hysteresis model in EMTP/ATP simulation," in *Power Engineering Conference, 2005*, vol. 2, 2005, pp. 653–656.